

Silk reinforced with graphene or carbon nanotubes spun by spiders

Emiliano Lepore¹, Francesco Bonaccorso^{2,3}, Matteo Bruna², Federico Bosia⁴, Simone Taioli^{5,6}, Giovanni Garberoglio⁵, Andrea. C. Ferrari², Nicola Maria Pugno^{1,7,8*}

¹ *Laboratory of Bio-inspired & Graphene Nanomechanics, Department of Civil, Environmental and Mechanical Engineering, University of Trento, Via Mesiano 77, 38123 Trento, Italy.*

² *Cambridge Graphene Centre, University of Cambridge, 9 JJ Thomson Avenue, CB3 0FA, Cambridge UK.*

³ *Istituto Italiano di Tecnologia, Graphene Labs, Via Morego 30, 16163 Genova, Italy.*

⁴ *Department of Physics and “Nanostructured Interfaces and Surfaces” Centre, Università di Torino, Via P. Giuria 1, 10125, Torino, Italy.*

⁵ *European Centre for Theoretical Studies in Nuclear Physics and Related Areas (ECT*), Bruno Kessler Foundation & Trento Institute for Fundamental Physics and Applications (INFN-TIFPA), Trento, Italy.*

⁶ *Faculty of Mathematics and Physics, Charles University, Prague, Czech Republic.*

⁷ *Centre of Materials and Microsystems, Bruno Kessler Foundation, Via Santa Croce 77, 38122 Trento, Italy.*

⁸ *School of Engineering and Materials Science, Queen Mary University, Mile End Road, London E1 4NS, UK.*

**Corresponding author: nicola.pugno@unitn.it*

The protein matrix and hard tissues of insects^{1,2,3,4}, worms^{5,6,7}, ants⁸ and spiders^{9,10} naturally incorporates metals, such as zinc^{1,2,3,5,8,9,10}, manganese^{2,3,9} and copper^{6,7}. This leads to mechanical hardening of teeth⁹, jaws^{5,6,7}, mandibles^{1,2,3,4,8}, ovipositors⁸ and to an enhancement of silk toughness¹⁰. Thus, the artificial incorporation of metals, or even insulating or semiconducting materials, into these protein structures could be exploited to obtain a reinforced matrix. A number of groups reported the introduction of metals, such as zinc^{1,2,3,5,8,9}, titanium¹⁰, aluminium⁵, copper^{6,7} and lead⁶ in the protein structure of spider silk through multiple pulsed vapour-phase infiltrations¹⁰. This allowed to increase its toughness modulus from 131 MPa⁸ up to 1.5 GPa¹⁰. Biomaterials with increased mechanical or conductive properties could find innovative applications in garment textiles¹¹ and medical nerve regeneration¹². It was suggested to coat spider silks with amine-functionalized multi-wall carbon nanotubes, to produce electrically conducting fibres⁹, or with cadmium telluride¹³, magnetite¹ or gold^{1,2} nanoparticles, for fluorescent¹³, magnetic^{13,14} and electronic applications^{13,15}. However, to the best of our knowledge, the incorporation of materials in the inner protein structure of spider silk has not been achieved to date. Here, we report the production of silk incorporating graphene and carbon nanotubes directly by spider spinning, after spraying spiders with the corresponding aqueous dispersions. We observe a significant increment of the mechanical properties with respect to the pristine silk, in terms of fracture strength, Young's and toughness moduli. We measure a fracture strength up to ~5.4 GPa, a Young's modulus up to ~47.8 GPa and a toughness modulus up to ~2.1 GPa, or 1567 J/g, which, to the best of our knowledge, is the highest reported to date, even when compared to the current toughest knotted fibres⁸. This approach could be extended to other animals and plants and could lead to a new class of bionic materials for ultimate applications.

Silkworm silks have been widely used by mankind for millennia. Although over 40,000 spider species have been classified to date^{16,17,18,19,20}, spider silks have been extensively studied only during the last decades^{21,22}, with an increasing number of publications and patents focusing on their outstanding mechanical^{23,24}, conducting^{2,14}, electrical^{13,15}, biocompatibility^{12,25,26} and low immunogenic¹⁹ properties⁶. These make silk potentially important for many applications, from garment textiles^{11,19,20} to electrical²¹, sensor^{13,14,15} and actuating^{15,23} devices or medical applications^{19,27,28} such as suture threads²⁹, biomimetic muscles¹⁶, nerve regeneration¹², ligament tissue repair¹⁹, scaffolds^{7,20}, up to long term applications such as flak jackets (currently limited by silk's large deformability)^{3,4,6,9}.

Silk is one of the keys to spider's evolutionary success¹⁰ and has been perfected over 400million years of evolution^{17,30}. Spider silk is generally described as a semi-crystalline biocompatible composite biopolymer^{12,19} and comprises the amino acids alanine, glycine and serine, organized into semi-amorphous helical-elastic α -chains and β -pleated nanocrystals^{6,7,9,19,21}. Spider silk is considered the best amongst spun polymer fibres^{5,8} in terms of tensile strength and strain, therefore toughness modulus, even when compared with the best performing synthetic fibres, such as ultra-high molecular weight polyethylene or poly(p-phenylene-2,6-benzobisoxazole)^{5,19}, or with moth silk, which originates from silkworms⁷. The mechanism of spider silk spinning involves a number of biological^{25,26}, chemical^{24,28,31} and physical²⁴, processes¹⁷, leading to silk fibres with a Young's modulus $\sim 10\text{GPa}$ ³² and fracture strength of approximately 1 GPa for dragline silk⁵.

Unlike the case of the largely available silkworm silks, large-scale spider farming and synthetic production of spider silk still remain to be achieved, due to its complex structure⁶ and the territorial and cannibalistic nature of spiders^{19,30}. Moreover, naturally spun fibres²⁴, obtained by forcible spinning^{20,33,34}, harvesting¹⁹ or extracting spidroin from glands³⁵, have reduced mechanical characteristics with respect to naturally-spun ones³⁴ (e.g. the Young's modulus is 11.1 GPa³³ (10.4 GPa³⁴) instead of 6.9 GPa³³ (9.2 GPa³⁴), the ultimate strain is 0.2%³³ (0.33%³⁴) instead of 0.3%³³ (0.47%³⁴) and the stress is 1.2 GPa³³ instead of 0.6 GPa³⁴, due to the CO₂ anaesthesia of spiders³³ and the consequent loss of active control of their silk spinning³⁴. Research to improve the mechanical^{6,23}, conductive^{2,14} or magnetic¹⁴ properties of spider silk has been limited^{14,15,21}. This is due to the difficulty of developing an adequate spinning methodology, balancing extrusion, drawing, yield and purity¹⁹. From a technological point of view¹⁹, wet-spinning³⁶, electro-spinning^{37,38}, hand-drawing^{39,40} or microfluidics approaches¹⁵ have been investigated to produce an artificial silk biomaterial at lab scale^{36,37,38,39,40}, mechanically, structurally or chemically modified with respect to natural one^{19,20}. Attempts to improve or modify the mechanical, magnetic and electrical properties of spider silk have been reported, using techniques such as melt-spinning¹¹, templating¹⁴, powder coating^{1,6,9,25}, atomic layer deposition⁵ and iodine doping², but they remain to be adequately perfected, especially at large scale, using naturally spun spider silk fibres.

Here, we study silk directly spun by spiders produced after the exposure of spiders to dispersions of carbon nanotube (CNTS) or graphene (GS). We find that the resulting silk has improved mechanical properties: a fracture strength up to $\sim 5.4\text{GPa}$, a Young's modulus up to $\sim 47.8\text{GPa}$, and an toughness modulus up to $\sim 2.1\text{GPa}$. This is the highest toughness modulus for a fibre, surpassing synthetic polymeric high performance fibres (e.g. Kelvar49TM 30) and even the current toughest knotted fibers⁸.

Two types of SWNTs are used in this study. The first is CoMoCAT SWNTs (named SWNT-1). The second is electric arc discharge SWNT (P2) from Carbon solutions inc. (named SWNT-2). SWNT dispersions are prepared by adding 1mg/10ml weight to volume ratio of each SWNT source to an aqueous solution of 2% w/v sodium deoxycholate (SDC, Sigma-Aldrich) in deionised water (DIW). De-bundling is obtained via ultrasonication using a Branson Ultrasonic Processor for 2 hours (450 kW at 20 kHz). The dispersions are ultracentrifuged using a TH-641 swinging bucket rotor in a Sorvall WX-100 ultracentrifuge at 200,000 x g for 2 hours at 18°C to remove SWNT bundles and other impurities, such as amorphous carbon, catalyst residuals, etc⁴¹.

The supernatant of the two dispersions after the ultracentrifugation step is collected using pipettes and used for the characterization. Graphite flakes are sourced from Sigma Aldrich Ltd. 100mg are dispersed in 10ml water with 2% v/w SDC. The dispersion is then ultrasonicated for 10 hours and subsequently ultracentrifuged, exploiting sedimentation-based separation (SBS) using a TH-641 swinging bucket rotor in a Sorvall WX-100 ultracentrifuge at 5000 rpm for 30 mins. After ultracentrifugation, the supernatant is extracted by pipetting. The concentration of graphitic flakes is determined from the optical absorption coefficient at 660nm, as described in Ref.42. A full optical and spectroscopic characterization of the samples is presented in Supplementary Information (S.I.)

Spiders were selected as described in S.I. Our silk fibres consist of multiple threads of approximately circular cross-section. An average diameter of the silk single thread is determined for each sample, at two different cross-sections along its length. This gives a nearly constant cross-sectional surface area along the fibre length. The number of threads in each fibre is also counted. The cross-sectional surface area of each fibre is calculated by multiplying the mean value of the cross-sectional area of the threads by their total number (*e.g.*, the mean cross-sectional area of threads of sample 1 is 0.202 μm^2 and the total number of threads is 15, resulting in a cross-sectional surface area of the fibre of sample 1 equal to 3.03 μm^2).

The presence of nanotubes and graphene is monitored by Raman spectroscopy. Fig. 1 compares the Raman spectra of the reference spider silk (RS) with that collected from spiders exposed to dispersions of graphene (GS) (Fig. 1b) and SWNTs (CNTS) (Fig. 1c,d). Fig. 1a shows an optical image of a suspended fibre. The RS Raman spectrum comprises several peaks in the 1000-1800 cm^{-1} and 2700-3500 cm^{-1} spectral regions. The peaks at ~ 1088 and 1160cm^{-1} are characteristic of the n(C-C) skeletal band of polypeptide chains^{16,26}. Two intense bands are also seen at $\sim 1230\text{cm}^{-1}$, characteristic of amide III groups in π -sheets structured proteins^{12,31} and at $\sim 1444\text{cm}^{-1}$ assigned to CH_2 bending modes, both bands typically found in the Raman spectrum of spider silk²⁴. The peaks at 1615cm^{-1} and 1665cm^{-1} are assigned to n(CO) amide I bands characteristic of the π -sheets configuration for the polypeptide backbone.^{12,24}. The Raman peaks in the region 2700-3500 cm^{-1} are typical of C-H and N-H vibrations³¹.

Raman spectra are also measured from GS and CNTS samples (see Fig. 2). The intensity of the different spectra is normalized with respect to the C-H band at $\sim 2934\text{cm}^{-1}$, the most intense in RS. The normalized RS spectrum is then subtracted from the GS and CNTS ones. Figs. 2a,b show that the spectrum of the graphene flakes in the dispersion is compatible with that of GS. At both 514 and 633nm, the D to G and 2D to G intensity ratios, $I(\text{D})/I(\text{G})$ and $I(2\text{D})/I(\text{G})$, as well as the positions of the G and 2D peaks, $\text{Pos}(\text{G})$ and $\text{Pos}(2\text{D})$, are very similar. The comparison indicates that graphene detected in GS has a similar level of disorder as the original material. The same holds for the case of CNTS. Figs 2c-f show that the spectra of the original SWNTs and those measured on CNTS are similar, indicating a negligible change in the structural properties.

Nanotensile tests are performed under controlled conditions as described in the S.I. Samples are subjected to traction up to failure at a constant strain rate of 0.1 %/s, consistently with previous studies on spider silk mechanics^{1,13,32}. The stress σ , ultimate strain ε , and Young's modulus E , are calculated as $\sigma = F/A_0$, $\varepsilon = \Delta l/l_0$, $E = d\sigma/d\varepsilon|_0$, where F is the force measured by our nanotensile system (see S.I. for details), A_0 is the cross-sectional surface area of the fibre, and Δl is the change in fibre length measured during the test. The area underlying the stress-strain curve corresponds to the energy per unit volume required to break the fibre²³, the so-called toughness modulus, also alternatively given in energy per unit mass, once the energy per unit volume is divided by the density of the material⁸. The variations of the mechanical properties of GS and CNTS with respect to RS are reported for each spider in Figs. 3a,b,c. Green bars indicate an enhancement of the mechanical properties, while red bars correspond to a decrease. The highest toughness modulus is $\sim 1567\text{ J/g}$, calculated assuming a mean silk density $\sim 1.34\text{ g/cm}^3$, see Fig. 4. The stress-strain curves of the silk fibres are presented in Fig. 5 and Fig. S6 in the S.I. The mean values of the Young's modulus, ultimate strain, fracture strength and toughness, are reported in Tables 1,2,3. The best mechanical performances are observed for the samples after the first collection (RDS_1). The

second collection (RDS_2) does not show mechanical enhancement with respect to the first or to RS, probably due to a physiological spider weakening during segregation, since neither additional food nor water were available during the experimental period, except SWNTs and graphene dispersions. In the cases marked with an asterisk in Figs. 5b,c, the second collection was impossible since the corresponding spiders died. Note that spider 5 died after the first treated dragline silk collection, but was able to spin the silk with the maximum increment in mechanical performance, whereas spider 7 spun the silk with the highest absolute values and survived.

Fracture strength, Young's modulus and toughness increase by a factors from 3 to 6 in CNTS and between 2 and 5 for GS. The highest fracture strength and Young's modulus increments are respectively of +731% (3.9 GPa) and +1183% (37.9 GPa) for CNTS, corresponding to an increment \sim +663% of toughness (1.1 GPa), with a decrement of 41% of ultimate strain (0.6 mm/mm). Note that the combination of increment in toughness and decrement in ultimate strain is very peculiar and fundamental in applications such as ballistic protection and flak jackets²⁰, where high performance textiles are required to stop bullets in millimeters⁴³. The second highest increments were of +350% (2.0 GPa) in fracture strength and +330% (19.3 GPa) in Young's modulus for SWNT-2-CNTS, corresponding to an increment of +204% in toughness (0.4 GPa), with a decrement of 36% of ultimate strain (0.3 mm/mm). A lower, but still significant, increment was observed for GS, with +151% (1.2 GPa) in fracture strength and +142% (13.0 GPa) in Young's modulus, corresponding to an increment of both toughness and ultimate strain of +250% (0.3 GPa) and +166% (0.4 mm/mm), respectively.

These data seem to be justified only by the presence of SWNTs or graphene within the bulk of the silk fibre, combined with a very efficient natural spinning/mixing mechanism. However, we cannot exclude the presence of SWNTs and graphene on the fibre silk surface as a result of spinning in an environment containing SWNT and graphene. However, such external coating on the fibre surface is not expected to significantly contribute to the observed mechanical strengthening, which we attribute to the inclusion of SWNTs and graphene within the fibre matrix.

The larger increments in the mechanical properties for CNTS could be due to the lateral characteristic dimensions of graphene flakes (\sim 200-300 nm), two orders of magnitude larger than the characteristic SWNT diameter, corresponding to a less efficient load transfer as resulting from (i) a longitudinal segment length of the flake not always longer than the critical length for maximal load transfer (as deduced by shear lag theory⁴⁴), (ii) a self-crumpled configuration of the flakes, (iii) a larger misalignment with respect to the SWNT case. Finding solutions for the three previously mentioned problems should enable us to obtain GS with mechanical properties superior to SWNTs, thanks to the two surfaces available for load transfer in graphene flakes⁴⁴. Tuning the constitutive law of the silk could also maximize the robustness of an entire structure²² and the insertion of knots has already been demonstrated to be a powerful tool for tuning the constitutive law of high-tough fibers⁸.

We perform atomistic simulations of GS and CNTS as a simple proof of concept by considering only one of the two copolymers present in the spider silk: major ampullate spidroin 2 (MASP2) (Figs. 6a,b), because it is the component delivering the major contribution to the stress-strain curve¹⁷. We stress that spider silks have a much more complex structure than modelled here. Nevertheless, the good agreement between computational results and experiments justifies this assumption. MASP2 forms random coil and helical structures and has a known primary sequence⁴⁵, as discussed in the S.I. The results are reported in Figs. 5c,d and show that the inclusion of SWNTs or graphene increases toughness with respect to the pristine MASP2 protein, the effect being larger in the presence of graphene. Inspection of the numerically generated molecular dynamics trajectories shows that the SWNT and graphene surround the protein and contrast the unfolding effect of the external force F .

Numerical simulations of the GS and CNTS mechanical properties are also performed, as discussed in S.I. To do this, a previously developed Hierarchical Fibre Bundle Model (HFBM)⁴⁶ was employed, whereby the macroscopic fibres are modelled as networks of micro-fibres and

reinforcements arranged in parallel and in series subjected to uniaxial tension, with statistically-distributed fracture strengths, according to measured or known input parameters for the constituents. The mechanical properties of the spider silk were derived from mean values in experimental measurements on RS, while those of SWNTs and graphene were obtained from literature^{47,48}. Simulations are used to estimate the equivalent volume fractions (V_f) of reinforcements obtained in the treated silk fibres. As a reference, comparisons are made with basic rules of mixtures (RM)⁴⁸. The calculated E , σ and ε values are compared to experimental results in Fig. 7. This shows that the equivalent volume fractions in GS and SWNTs vary between 1% (sample 15) and 15% (sample 7), with an average of 6.9%.

In summary, spiders placed in an environment with water solutions of nanotubes or graphene produce dragline silk with unprecedented mechanical properties, realizing the toughest achieved fibers, with a strength only comparable with that of the strongest carbon fibers or that of the limpet teeth⁴⁹. Knots could further increase the toughness⁸. Spiders could spin graphene and nanotubes in the silk also as an efficient way of eliminating them from their organism. Spider natural and very efficient spinning can thus allow the collection of the most performing silk fiber when compared to synthetic recombinant silks, which represents the most promising silk material to be efficiently reinforced. This new reinforcing procedure could also be applied to other animals and plants, leading to a new class of bionic materials for ultimate applications.

Acknowledgments

We acknowledge “Nanofacility Piemonte” at the INRIM Institute for the FESEM, a Newton International Fellowship, a Royal Society Wolfson Research Merit Award, EPSRC grants EP/K01711X/1, EP/K017144/1, EP/L016087/1. N.M.P. is supported by the European Research Council (ERC StG Ideas 2011 BIHSNAM no. 279985 on ‘Bio-inspired hierarchical supernanomaterials’, ERC PoC 2013-1 REPLICA2 no. 619448 on ‘Large-area replication of biological anti-adhesive nanosurfaces’, ERC PoC 2013-2 KNOTOUGH no. 632277 on ‘Super-tough knotted fibres’), by the European Commission under the Graphene Flagship (WP10 ‘Nanocomposites’, no. 604391) and by the Provincia Autonoma di Trento (‘Graphene nanocomposites’, no. S116/2012-242637 and reg. delib. no. 2266).”. This paper is dedicated to the memory of prof. Franco Montevicchi.

Author contributions

N.M.P. had the idea, designed and supervised the entire research and analyzed the results. E.L. collected the silk and performed the tensile tests. Fr. B. provided and characterized the graphene and carbon nanotube solutions. M.B. performed the Raman analysis, Fe. B. performed the hierarchical fibre bundle simulations. S.T. and G.G. performed the atomistic simulations. A.C.F. analyzed the Raman results. N.M.P. and E.L. drafted the manuscript and all authors contributed to the writing of its final version.

References

- 1 Mayes, E. L., Vollrath F. & Mann, S. Fabrication of magnetic spider silk and other silk-fiber composites using inorganic nanoparticles. *Adv. Mater.* **10**, 801–805 (1998).
- 2 Steven, E. *et al.* Physical characterization of functionalized spider silk: electronic and sensing properties. *Sci. Technol. Adv. Mater.* **12**, 055002 (2011).

- 3 Brunetta, L. & Craig, C. L. Spider Silk, Evolution and 400 million years of spinning, waiting, snagging, and mating. *Csiro Publishing* (2010).
- 4 Porter, D. & Vollrath, F. Silk as a biomimetic ideal for structural polymers. *Adv. Mater.* **21**, 487–492 (2009).
- 5 Lee, S. M. *et al.* Greatly increased toughness of infiltrated spider silk. *Science* **324**, 488–492 (2009).
- 6 Silva, L. P. & Rech E. L. Unravelling the biodiversity of nanoscale signatures of spider silk fibres. *Nat. Commun.* **4**, 3014 (2013).
- 7 Dal Pra, I., Chiarini, A., Boschi, A., Freddi, G. & Armato, U. Novel dermo-epidermal equivalents on silk fibroin-based formic acid-crosslinked three-dimensional nonwoven devices with prospective applications in human tissue engineering/regeneration/repair. *Int. J. Mol. Med.* **18**, 241–247 (2006).
- 8 Pugno, N. M. The “Egg of Columbus” for making the world's toughest fibres. *PLoS ONE* **9** (4), e93079 (6 pp.) (2014).
- 9 Steven, E. *et al.* Carbon nanotubes on a spider silk scaffold. *Nat. Commun.* **4**, 2435 (2013).
- 10 Sensenig, A., Agnarsson, I. & Blackledge, T. A. Behavioural and biomaterial coevolution in spider orb webs. *J. Evolution. Biol.* **23**, 1839–1856 (2010).
- 11 Moore, E. M., Ortiz, D. L., Marla, V. T., Shambaugh, R. L. & Grady, B. P. Enhancing the strength of polypropylene fibers with carbon nanotubes. *J. Appl. Polym. Sci.* **93**, 2926–2933 (2004).
- 12 Williams, A. C., Barry, B. W. & Edwards, H. G. M. Comparison of Fourier transform Raman spectra of mammalian and reptilian skin. *Analyst* **119**, 563–566 (1994).
- 13 Swanson, B. O., Blackledge, T. A. & Hayashi, C. Y., Spider capture silk: performance implications of variation in an exceptional biomaterial. *J. Exp. Zool.* **307A**, 654–666 (2007).
- 14 Dionigi, C. *et al.* A nanostructured conductive bio-composite of silk fibroin-single walled carbon nanotubes. *J. Mater. Chem. B* **2**, 1424–1431 (2014).
- 15 Heim, M., Keerl, D. & Scheibel, T. Spider silk: from soluble protein to extraordinary fiber. *Angew. Chem. Int. Ed.* **48**, 3584–3596 (2009).
- 16 Colomban, P., Dinh, H. M., Riand, J., Prinsloo, L. C. & Mauchamp, B. Nanomechanics of single silkworm and spider fibres: a Raman and micro-mechanical in situ study of the conformation change with stress. *J. Raman Spectrosc.* **39**, 1749–1764 (2008).
- 17 Foelix, R. F. *Biology of Spiders*, Oxford University Press (1996).
- 18 Agnarsson, I., Kuntner, M. & Blackledge, T. A. Bioprospecting finds the toughest biological material: extraordinary silk from a giant riverine orb spider. *PLoS ONE* **5**, e11234 (2010).
- 19 Hardy, J. G., Römer, L. M. & Scheibel, T. R. Polymeric materials based on silk proteins. *Polymer* **49**, 4309–4327 (2008).

- 20 Thiel, B. L. & Viney, C. Spider major ampullate silk (drag line): smart composite processing based on imperfect crystals. *J. Microsc.* **185**, 179–187 (1997).
- 21 Keten, S. & Buehler, M. J. Nanostructure and molecular mechanics of dragline spider silk protein assemblies. *J. R. Soc. Interface* **7**, 1709–1721 (2010).
- 22 Cranford, S. W., Tarakanova, A., Pugno, N. M. & Buehler, M. J. Nonlinear material behaviour of spider silk yields robust webs. *Nature* **482**, 72–78 (2012).
- 23 Lepore, E., Marchioro, A., Isaia, M., Buehler, M. & Pugno, N. Evidence of the most stretchable egg sac silk stalk, of the European spider of the year *Meta Menardi*. *PLoS ONE* **7**, 1–12 (2012).
- 24 Shao, Z., Vollrath, F., Sirichaisit, J. & Young, R. J. Analysis of spider silk in native and supercontracted states using Raman spectroscopy. *Polymer* **40**, 2493–2500 (1999).
- 25 Chu, M. & Sun, Y. Self-assembly method for the preparation of near-infrared fluorescent spider silk coated with CdTe nanocrystals. *Smart Mater. Struct.* **16**, 2453–2456 (2007).
- 26 Edwards, H. G. M. & Farwell, D. W. Raman-spectroscopic studies of silk. *J. Raman Spectrosc.* **26**, 901–909 (1995).
- 27 Brown, C. P. *et al.* The critical role of water in spider silk and its consequence for protein mechanics. *Nanoscale* **3**, 3805–3811 (2011).
- 28 Blackledge, T. A. & Hayashi, C. Y. Silken toolkits: biomechanics of silk fibers spun by the orb web spider *Argiope argentata* (Fabricius 1775). *J. Exp. Biol.* **209**, 2452–2461 (2006).
- 29 Sahni, V., Labhasetwar D. V. & Dhinojwala A. Spider silk inspired functional microthreads. *Langmuir* **28**, 2206–2210 (2012).
- 30 Vendrely, C. & Scheibel T. Biotechnological production of spider-silk proteins enables new applications. *Macromol. Biosci.* **7**, 401–409 (2007).
- 31 Sokrates, G. Infrared and Raman characteristic group frequencies: tables and charts. *Colloid. Polym. Sci.* **283**, 235 (2004).
- 32 Hayashi, C. Y., Blackledge, T. A. & Lewis, R. V. Molecular and mechanical characterization of aciniform silk: uniformity of iterated sequence modules in a novel member of the spider silk fibroin gene family. *Mol. Biol. Evol.* **21**, 1950–1959 (2004).
- 33 Guinea, G. V., Elices, M., Real, J. I., Gutierrez, S. & Perez-Rigueiro J. Reproducibility of the tensile properties of spider (*Argiope trifasciata*) silk obtained by forced silking. *J. Exp. Zool.* **303**, 37–44 (2005).
- 34 Blackledge, T. A., Swindeman, J. E. & Hayashi, C.Y. Quasistatic and continuous dynamic characterization of the mechanical properties of silk from the cobweb of the black widow spider *Latrodectus Hesperus*. *J. Exp. Biol.* **208**, 1937–1949 (2005).

- 35 Andersen, S. O. Amino acid composition of spider silks. *Comp. Biochem. Phys.* **35**, 705–711 (1970).
- 36 Islam, S. *et al.* Methods and apparatus for spinning spider silk proteins. US Patent 7,057,023. Nexia Biotechnologies Inc.; 2006.
- 37 Jin, H. J., Fridrikh, S. V., Rutledge, G. C. & Kaplan D. L. Electrospinning *Bombyx mori* silk with poly(ethylene oxide). *Biomacromolecules* **3**, 1233–1239 (2002).
- 38 Wang, H., Zhang, Y. P., Shao, H. L. & Hu, X. C. Electrospun ultra-fine silk fibroin fibers from aqueous solutions. *J. Mater. Sci.* **40**, 5359–5363 (2005).
- 39 Shao, Z., Yang, Y. & Vollrath, F. Structure and behaviour of regenerated spider silk. *Macromolecules* **36**, 1157–1161.
- 40 Teule, F., Furin, W. A., Cooper, A. R., Duncan, J. R. & Lewis, R. V. Modifications of spider silk sequences in an attempt to control the mechanical properties of the synthetic fibers. *J. Mater. Sci.* **42**, 8974–8985 (2007).
- 41 Bonaccorso, F. *et al.* Density gradient ultracentrifugation of nanotubes: interplay of bundling and surfactants encapsulation. *J. Phys. Chem. C* **114**, 17267–17285 (2014).
- 42 Torrisi, F. *et al.* Inkjet-printed graphene electronics. *ACS Nano* **6**, 2992 (2012).
- 43 Lin, C.-C., Lin, J.-H. & Chang, C.-C. Fabrication of Compound Nonwoven Materials, for Soft Body Armor. *J. Forensic. Sci.* **56**, 1150–1155 (2011).
- 44 Pugno, N. M. Towards the Artsutanov’s dream of the space elevator: the ultimate design of a 35GPa stronger tether thanks to graphene. *Acta Astronautica* **82**, 221–224 (2013).
- 45 Keten, S. & Buehler, M. J. Nanostructure and molecular mechanics of spider dragline silk protein assemblies. *J. R. Soc. Interface* **7**, 1709–1721 (2010).
- 46 Pugno, N. M., Borgia, F. & Carpinteri A. Multiscale stochastic simulations for tensile testing of nanotube-based macroscopic cables. *Small* **4**, 1044–1052 (2008).
- 47 Ruoff, R. S., Qian, D. & Liu, W. K. Mechanical properties of carbon nanotubes: theoretical predictions and experimental measurements. *C. R. Physique* **4**, 993–1008 (2003).
- 48 Lee, C., Wei, X., Kysar, J. W. & Hone, J. Measurement of the elastic properties and intrinsic strength of monolayer graphene. *Science* **321**, 385–388 (2008).
- 49 Barber A. H., Lu D., Pugno N. Extreme strength observed in limpet teeth. *J. R. Soc. Interface.* **12**, 20141326 (2015).

TABLES

Table 1. Mechanical properties (average values) of RS samples.

Spider n.	Young's Modulus (GPa)	Ultimate Strain (mm/mm)	Fracture Strength (MPa)	Toughness Modulus (MPa)
1	6.0	0.288	795.2	128.2
2	27.3	0.578	2397.2	713.0
3	13.4	0.464	1257.5	422.6
4	1.9	1.381	465.1	235.6
5	3.2	1.017	534.7	172.4
6	37.1	0.278	4045.9	732.1
7	15.1	0.394	1726.6	476.4
8	2.1	0.689	179.7	61.1
9	5.9	0.534	580.7	205.3
10	3.0	0.551	281.2	75.3
11	24.3	0.745	1969.1	764.7
12	3.1	0.769	173.4	48.9
13	5.5	0.879	648.6	320.3
14	3.8	1.708	364.0	247.8
15	9.2	0.256	825.2	101.8

Table 2. Mechanical properties (average values) of the first collection of silk samples produced after exposure of the spiders to the SWNT or graphene dispersions (Spiders n. 1-6 with SWNT-1, spiders n. 7-10 with SWNT-2, spiders n. 11-15 with graphene). The largest increments in the silk mechanical properties are observed for spider 5 whereas the highest absolute values are observed for spider 7.

Spider n.	Young's Modulus (GPa)	Ultimate Strain (mm/mm)	Fracture Strength (MPa)	Toughness Modulus (MPa)
1	3.9	0.622	326.1	66.7
2	40.1	0.200	3914.6	587.2
3	8.7	0.678	1195.8	387.0
4	2.4	0.946	579.4	187.6
5	37.9	0.598	3907.2	1144.0
6	9.6	0.498	954.3	210.2
7	47.8	0.749	5393.5	2143.6
8	3.1	0.406	315.7	47.8
9	19.3	0.342	2034.9	419.8
10	0.2	0.319	20.1	2.6
11	0.8	0.331	58.0	7.9
12	4.9	0.430	607.5	148.5
13	3.1	0.519	421.8	130.3
14	0.4	0.288	45.9	6.0
15	13.0	0.426	1245.6	254.7

Table 3. Mechanical properties (average values) of the second collection of silk samples produced after exposure of the spiders to the SWNT and graphene dispersions. 26% of the spiders died between the first and second collections, thus the corresponding data are absent.

Spider n.	Young's Modulus (GPa)	Ultimate Strain (mm/mm)	Fracture Strength (MPa)	Toughness Modulus (MPa)
1	2.8	0.423	275.1	55.3
2	9.5	0.368	906.2	168.1
3	5.1	0.753	562.5	157.4
4	-	-	-	-
5	-	-	-	-
6	3.6	1.325	507.6	198.1
7	3.6	0.818	473.1	195.6
8	9.9	0.509	1222.8	196.9
9	-	-	-	-
10	1.4	1.055	211.2	99.6
11	8.6	0.540	1102.5	241.4
12	5.6	1.082	716.7	286.7
13	5.6	0.577	499.6	125.7
14	-	-	-	-
15	2.5	1.138	216.9	110.4

FIGURES

Figure 1: Optical characterization of dragline silk spun by spiders after exposure to nanotube or graphene dispersions. a) Optical picture of a spider silk fibre suspended by a mechanical support (left) and map of the 2D peak intensity overlapped to the optical picture of the spider silk spun by spiders after exposure to graphene (right). b) Raman spectra of RS (black line, at 514.5nm), GS at 514.5nm (green line) and 633nm (red line). Raman spectra of c) SWNT-1-CNTS d) SWNT-2-CNTS at 514.5nm (green line) and 633nm (red line) excitation wavelengths.

Figure 2: Raman spectra of original graphene and nanotube samples compared to those measured in RS and SWNTs. Raman spectra of graphene (black line) and GS (red line) at a) 514.5nm and b) 633nm. Raman spectra of c,d) SWNT-1, SWNT-2 and SWNT-1-CNTS and SWNT-2-CNTS at (c,e) 514.5nm and (d,f) 633nm excitation wavelengths.

Figure 3: Mechanical properties of dragline silk spun by spiders after exposure to nanotube or graphene dispersions. Percentage increment (green bars) or decrement (red bars) of the mechanical properties measured from neat dragline silk (RS) to the first collection of treated dragline silk samples with (a) SWNT-1-CNTS, (b) SWNT-2-CNTS or (c) GS. The symbol (*) specifies that spider died before the second collection.

Figure 4: Toughness modulus and strength of different materials and composites. Note the toughness record of the present silk and its high strength (only comparable to that of carbon fibers or limpet teeth⁴⁹). Also, knots in this silk could further increase its toughness thanks to the concept presented in ref. 8.

Figure 5: Stress-strain curves of the silks showing the highest mechanical properties. (a) Stress-strain curves of silks that showed the highest increments of the mechanical properties after the first (RDS_1) or second (RDS_2) collection for (b) SWNT-1, (c) SWNT-2 or (d) GS. The symbol (*) specifies that spiders died before the second collection.

Figure 6: Proof of concept via atomistic simulations of force-displacement curves. Arrangement of (a) SWNTs or (b) graphene around MASP2 and corresponding (c) force-displacement curves. Dependence of applied force end-to-end distance and (d) corresponding dissipated energy (here called toughness) for MASP2. We report the applied force F as a function of the end-to-end distance d , instead of the stress-strain curve, and its integral (energy) instead of the toughness modulus as we are working with a single MASP2 protein.

Figure 7: Comparison of experiments with HFBM simulations and direct or indirect rules of mixture (RM). RM predictions are shown as blue lines (direct RM law, taken as an upper bound for predictions) and as red lines (inverse RM law, taken as lower bound for the predictions). Experimental data are plotted as green triangles, with corresponding sample numbers, and with error bars corresponding to the experimental standard deviations (with V_f values estimated from RM or HFBM, as explained below), while HFBM data are shown as hollow diamonds, with error bars corresponding to uncertainties due to statistical variations in the simulations. Only experimental data compatible with a rule of mixtures V_f estimation. *i.e.*, with improved properties with respect to RS, are shown.

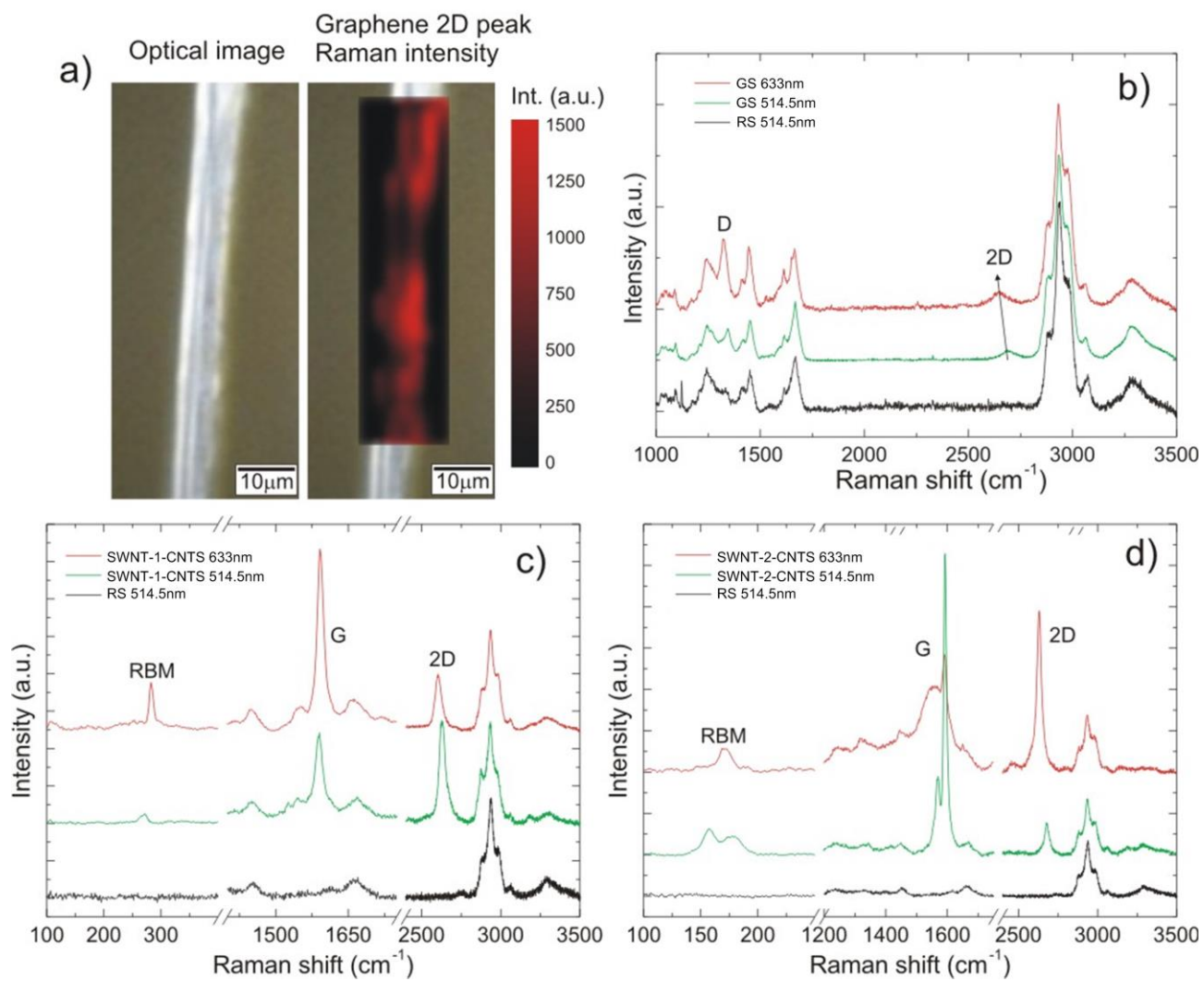


Figure 1

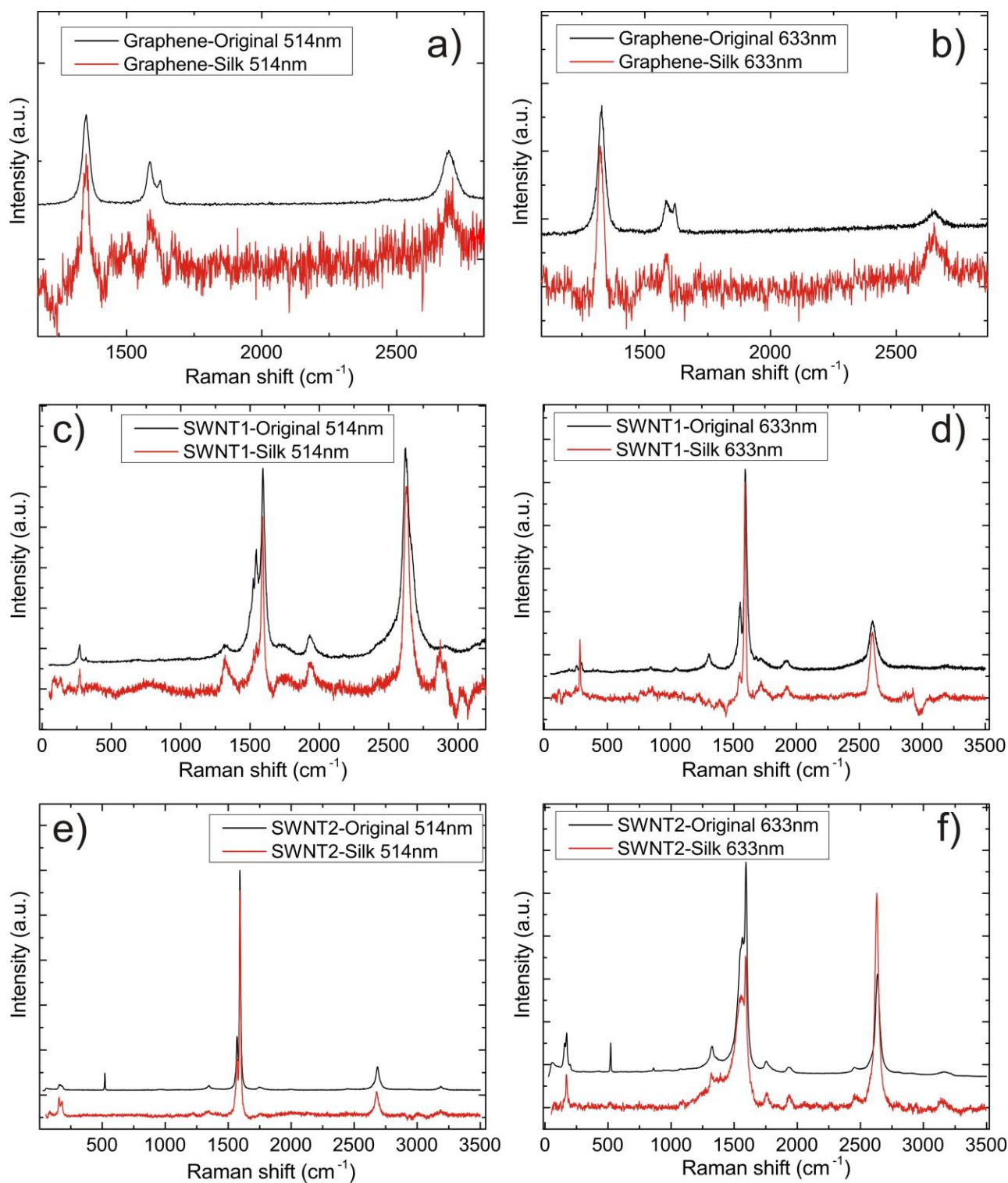
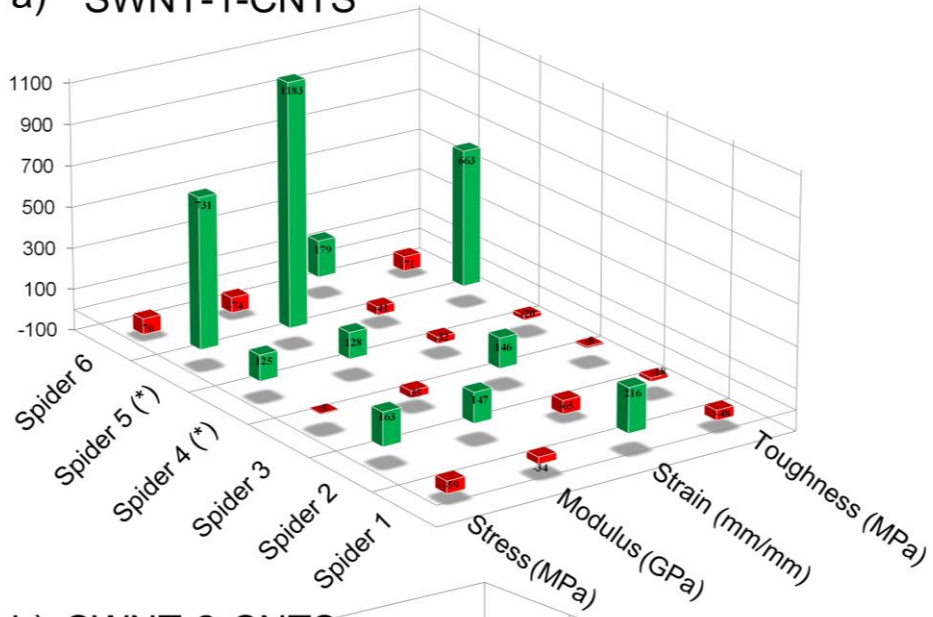
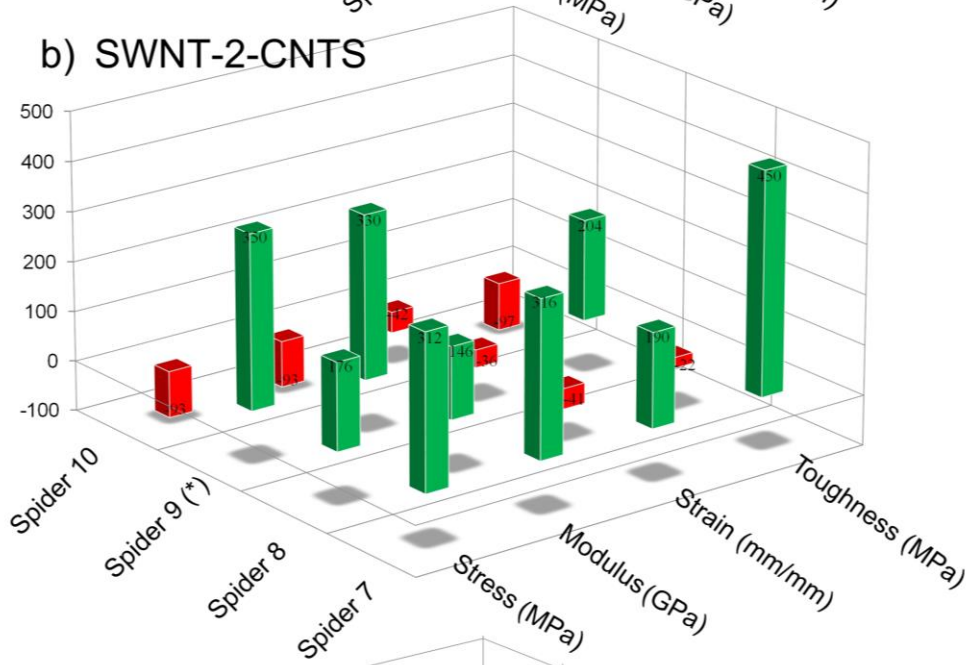


Figure 2.

a) SWNT-1-CNTS



b) SWNT-2-CNTS



c) GS

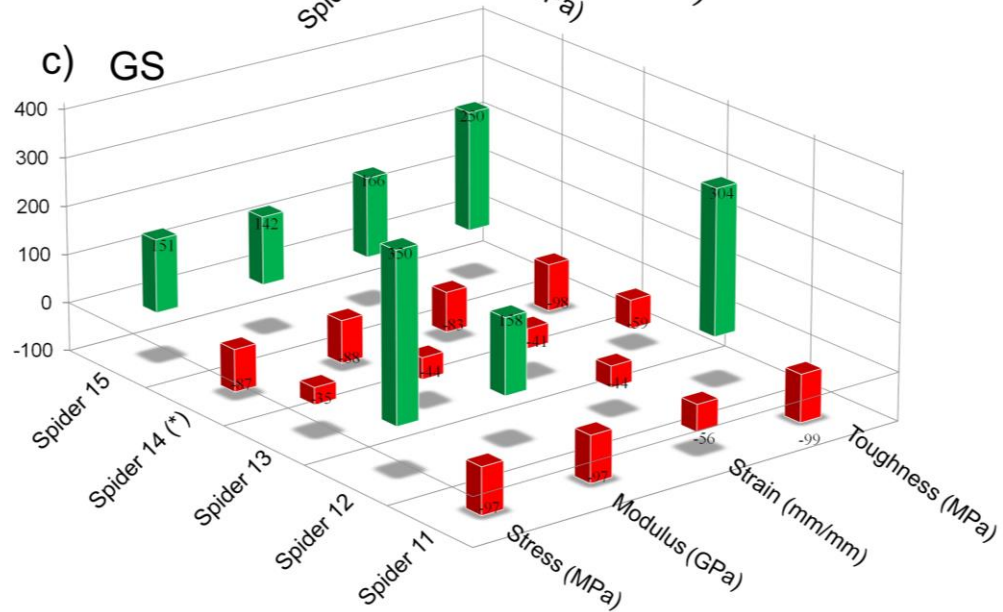


Figure 3

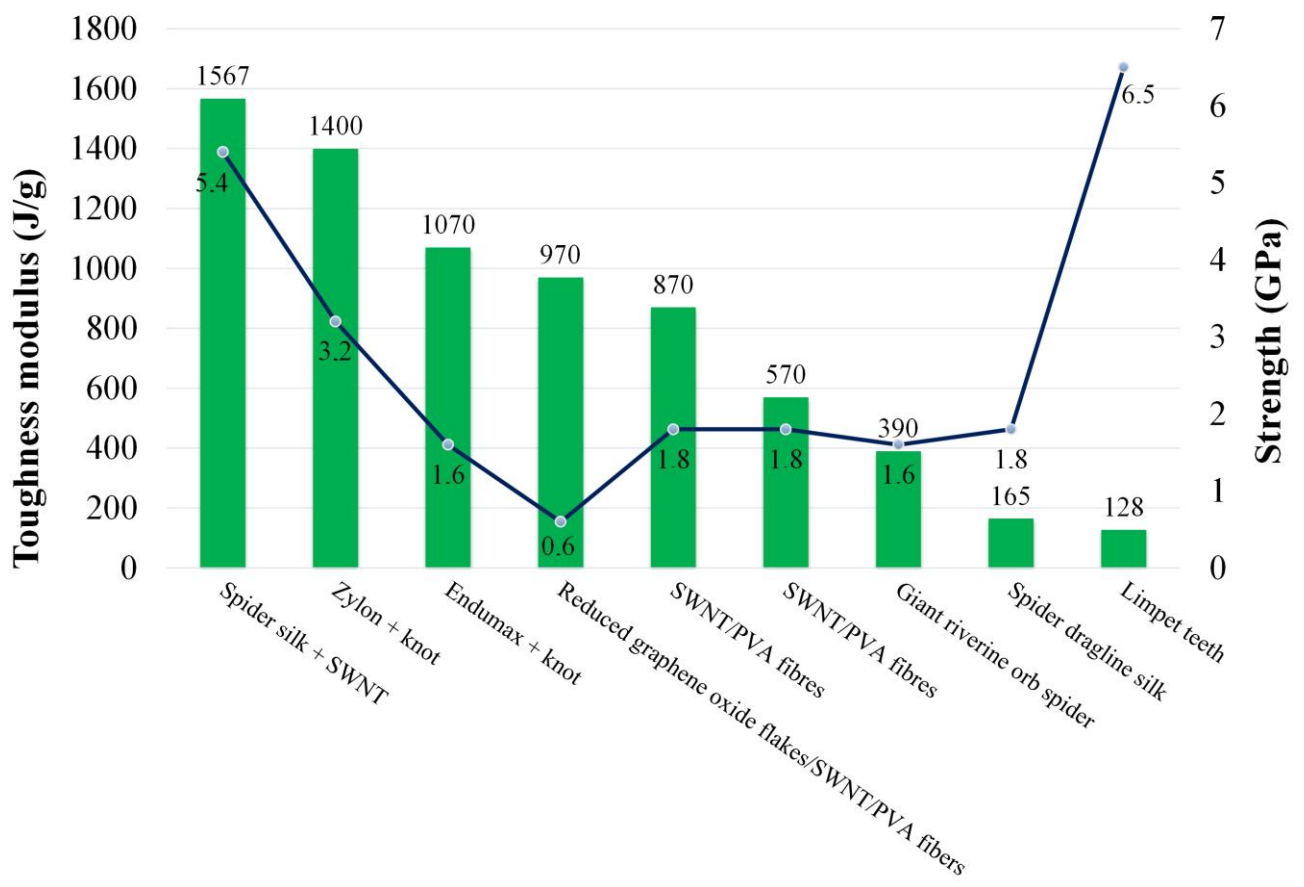


Figure 4

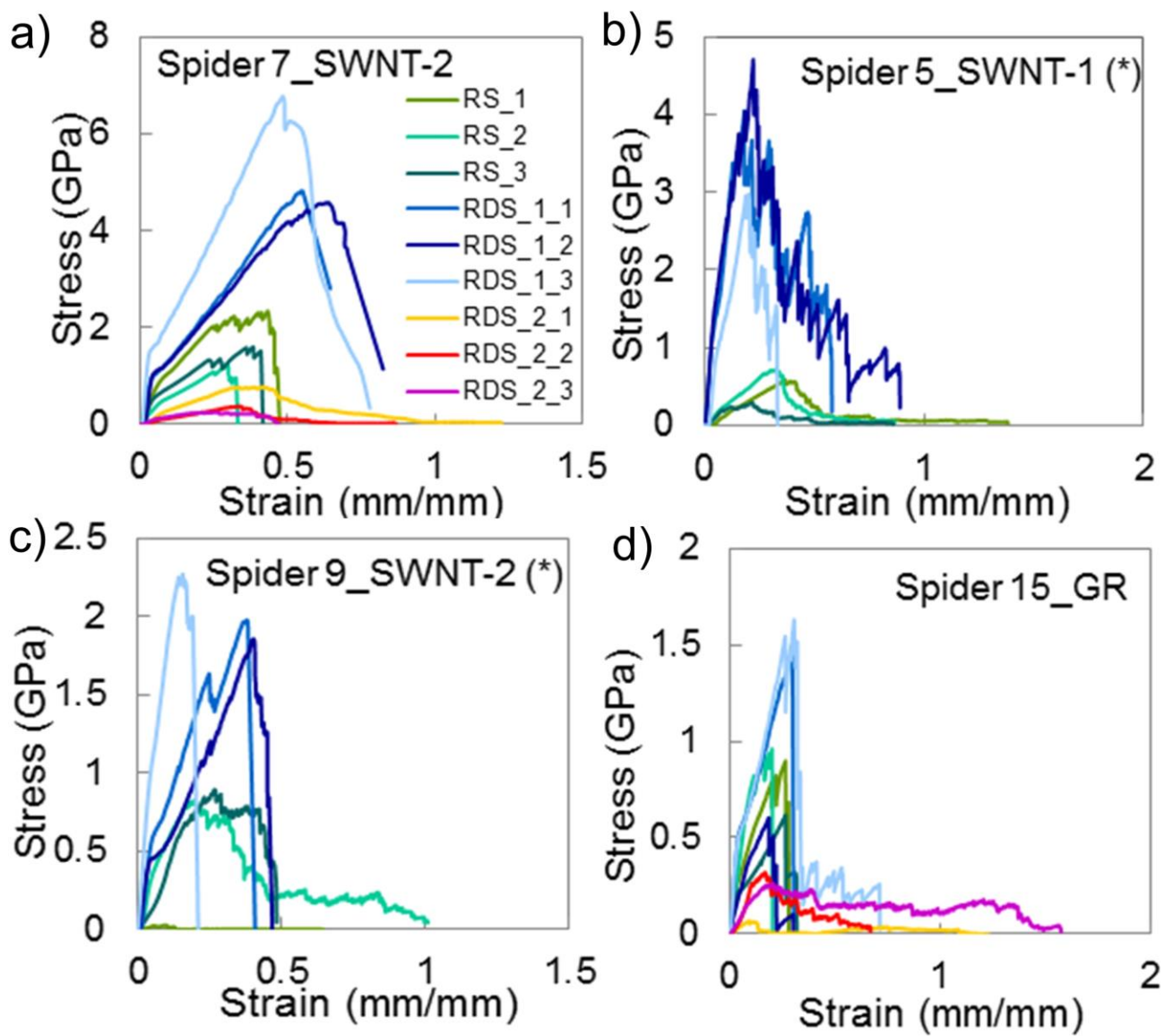


Figure 5

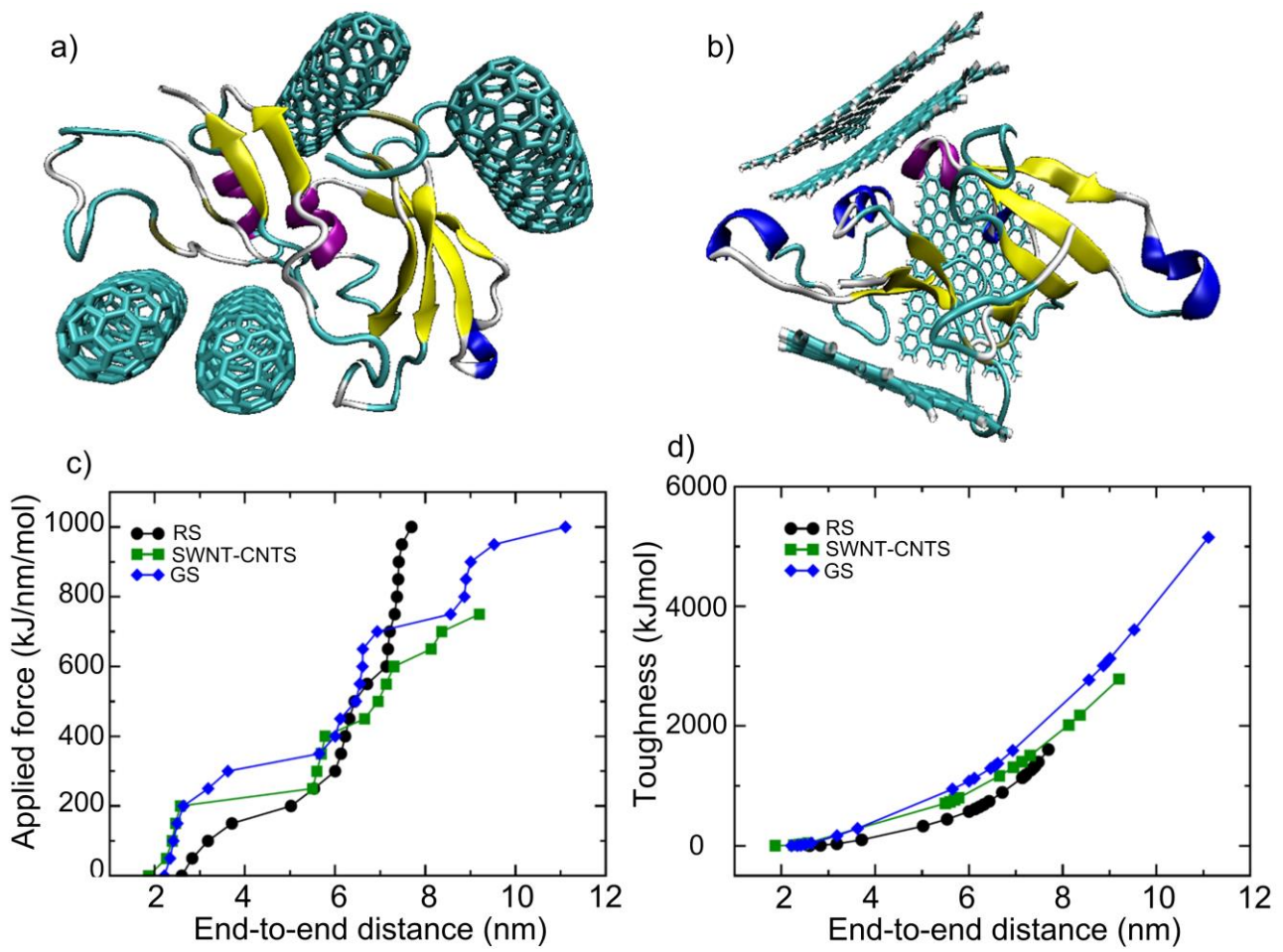


Figure 6

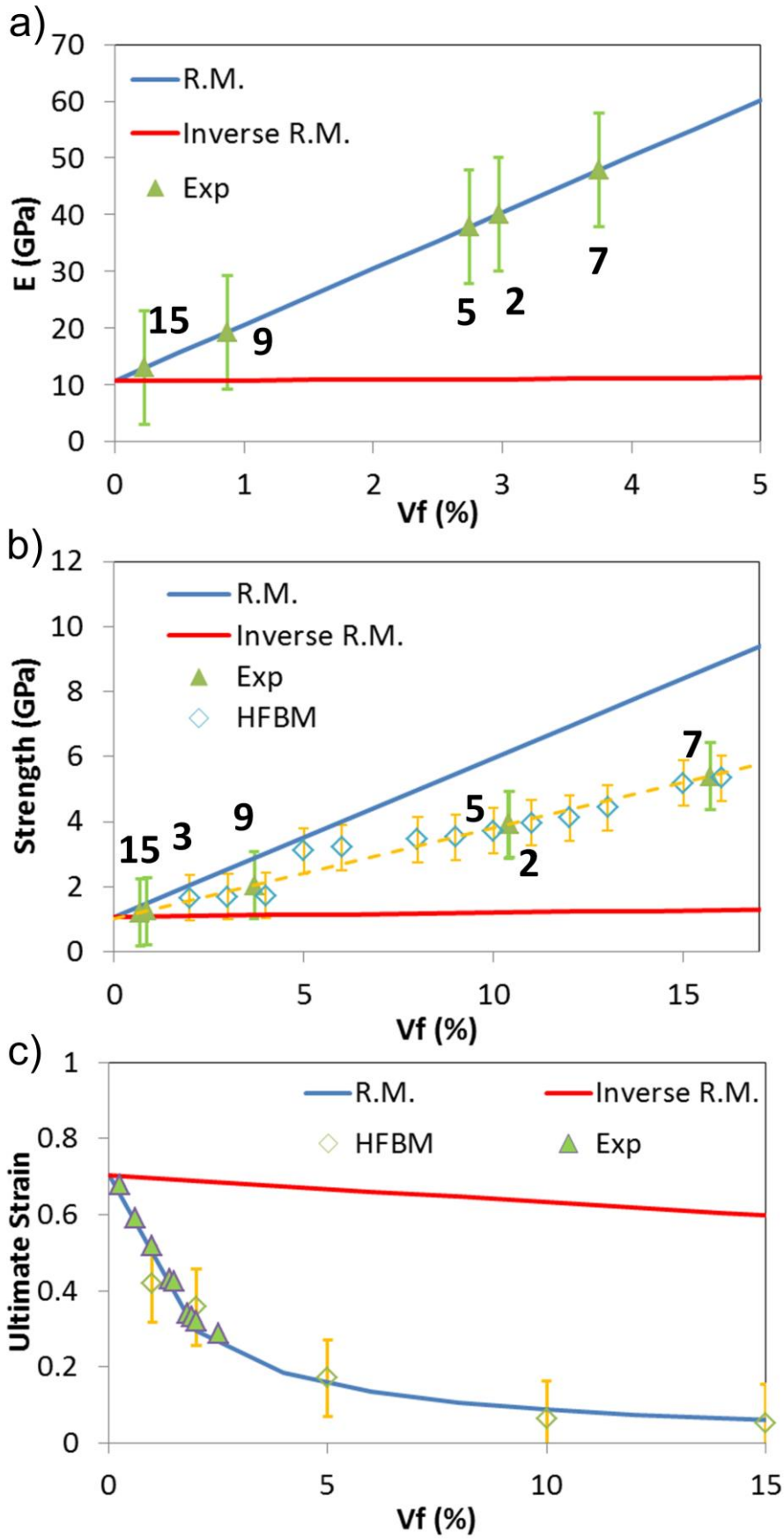


Figure 7

Silk reinforced with graphene or carbon nanotubes spun by spiders

Supplementary Informations

Emiliano Lepore¹, Francesco Bonaccorso^{2,3}, Matteo Bruna², Federico Bosia⁴, Simone Taioli^{5,6}, Giovanni Garberoglio⁵, Andrea. C. Ferrari², Nicola Maria Pugno^{1,7,8*}

¹ *Laboratory of Bio-inspired & Graphene Nanomechanics, Department of Civil, Environmental and Mechanical Engineering, University of Trento, Via Mesiano 77, 38123 Trento, Italy.*

² *Cambridge Graphene Centre, University of Cambridge, 9 JJ Thomson Avenue, CB3 0FA, Cambridge UK.*

³ *Istituto Italiano di Tecnologia, Graphene Labs, Via Morego 30, 16163 Genova, Italy.*

⁴ *Department of Physics and “Nanostructured Interfaces and Surfaces” Centre, Università di Torino, Via P. Giuria 1, 10125, Torino, Italy.*

⁵ *European Centre for Theoretical Studies in Nuclear Physics and Related Areas (ECT*), Bruno Kessler Foundation & Trento Institute for Fundamental Physics and Applications (INFN-TIFPA), Trento, Italy.*

⁶ *Faculty of Mathematics and Physics, Charles University, Prague, Czech Republic.*

⁷ *Centre of Materials and Microsystems, Bruno Kessler Foundation, Via Santa Croce 77, 38122 Trento, Italy.*

⁸ *School of Engineering and Materials Science, Queen Mary University, Mile End Road, London E1 4NS, UK.*

S1. Collection of spiders

We randomly collected fifteen Pholcidae spiders (male and female of different ages). The sampling site was Torrente Chisone, between Macello and Garzigliana, Province of Torino, Italy (Geographical coordinates: 44.844 East, 7.385 North). Each spider was gently and individually segregated in a box of 19 x 12.5 x 7.5 cm³ with four air inlets, a transparent top, white bottom and lateral sides. Spiders were transferred within 3 days from capture under an extractor fan with controlled ambient condition temperature and humidity (21.0 ± 0.2 °C and 54.3 ± 0.7 %) in the MicroTechnologies Laboratory (Bruno Kessler Foundation, Trento, Italy) where they were kept during the entire experimental procedure.

After 5 days reference dragline silk samples (RS) were collected. Subsequently, spiders were exposed to aqueous dispersions of graphene and single wall carbon nanotubes (SWNTs), Fig S1. Nine spiders (1, 4, 5, 7, 9, 11, 13, 14, 15) started to spin silk after 2 days, while 6 took 12 days (2, 3, 6, 8, 10, 12). The dragline silk was then collected. Spiders 1-6 were treated with SWNT-1 and 7-10 with SWNT-2 (Fig. S1c), and 11-15 with graphene (Fig. S1d). After 42 days, dragline silk was collected for the second time. The silk is in the form of a single fiber composed of multiple threads. Multiple samples are obtained by cutting the fiber into 20mm-length strands for tensile tests and for the measurement of the cross-sectional area, following the procedure described in Ref. ². This suggested to take adjacent samples to ensure reproducibility of fiber properties and to use one out of five samples (instead of three as here) as control to measure the fiber cross-sectional area by Field Emission Scanning Electron Microscopy (FESEM). In our work, the cross-sectional area of the fiber is determined using a FESEM (FEI-InspectTM F50, at 5-10 kV) without sputter coating.

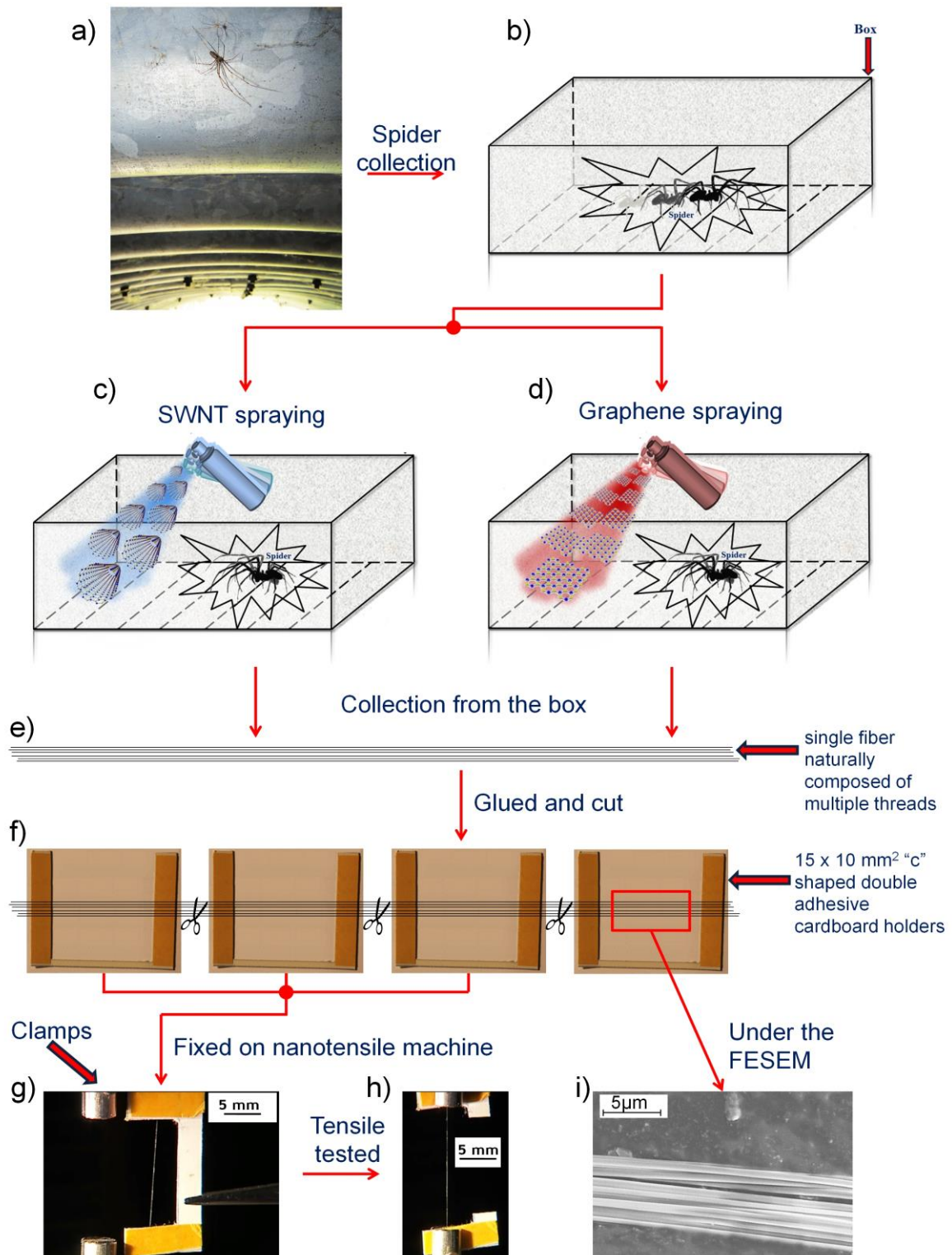


Figure S1: Schematic illustration of the experimental procedure. (a) Sampling site and experimental box for the collection of (b) neat dragline silk samples and, after spraying (c) nanotubes or (d) graphene aqueous dispersions, of treated dragline silk samples. (e) Collection of silk in the form of a single fibre, composed of multiple threads, from which multiple samples have been obtained by fixing the ends of the fibre to 15 x 10 mm² "c" shaped double adhesive cardboard holders and (f) cutting the fibre into four shorter pieces, (g) mounted on nanotensile machine clamps (h) for nanotensile tests and (i) for measuring the fibre cross-sectional surface area with a FESEM. Scale bar 5 μm.

S2. Characterization of graphene and SWNT dispersions

S2.1 Optical absorption Spectroscopy

S2.1.1 Optical absorption spectroscopy of SWNTs

Optical absorption spectroscopy (OAS) reveals various properties of SWNT dispersions such as transition energies,^{3,4,5} bundling^{3,4,6} and concentration.⁷

Optical absorption spectra were acquired in a Perkin Elmer 950 with 1nm resolution. Measurements were carried out in the range 400-1300nm, limited by the strong absorption features of water. However, this range is sufficient to cover the first and second excitonic transitions of s-SWNTs^{2,8,9} and the first transition of m-SWNTs, for CoMoCAT^{3,8,9} and the second and third transitions of s-SWNTs and first of m-SWNTs^{10,11} for the P2 samples. Absorption from solvent and surfactants is subtracted, by measuring solutions with only solvent and surfactant.

The assignment of the optical transitions is based on the empirical Kataura plot of Ref. 21. This gives values of optical transition frequencies versus chirality for SWNTs in aqueous surfactant dispersions, and is more appropriate than Kataura plots theoretically derived from tight binding and other models¹².

The OAS of SWNT-1 and SWNT-2 are reported in Fig. S2. SWNT-1 have sharper peaks with than SWNT-2 samples.

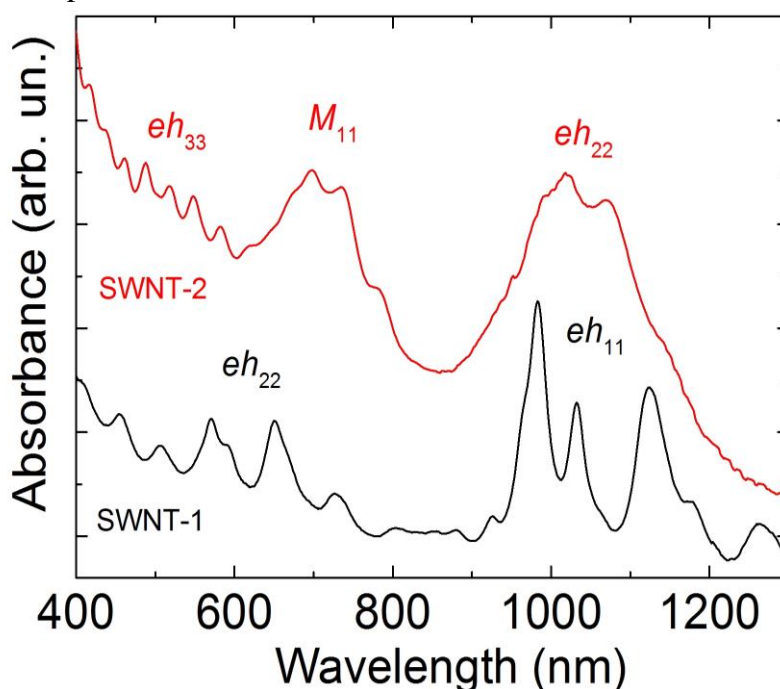


Figure S2: Absorption spectra of SWNT-1 (black curve) and SWNT-2 (red curve). The labels eh_{11} , eh_{22} , eh_{33} and M_{11} refer to the first, second, third semiconducting and the first metallic excitonic transition, and are a guide to the eye, since overlap between different excitonic transitions exists^{11,21}. The spectra are normalized for a clear visualization.

S2.1.1 Optical absorption spectroscopy of graphitic flakes

Fig. S3 report the absorption spectrum of the graphene dispersion. The peak at ~266 nm is a signature of the van Hove singularity in the graphene density of states.¹³ OAS used to evaluate the

concentration of graphitic material in dispersion, using the experimentally derived absorption coefficient of $1390\text{Lg}^{-1}\text{m}^{-1}$ at 660nm ^{14,15,16} we estimate concentration $\sim 0.03\text{mg/ml}$.

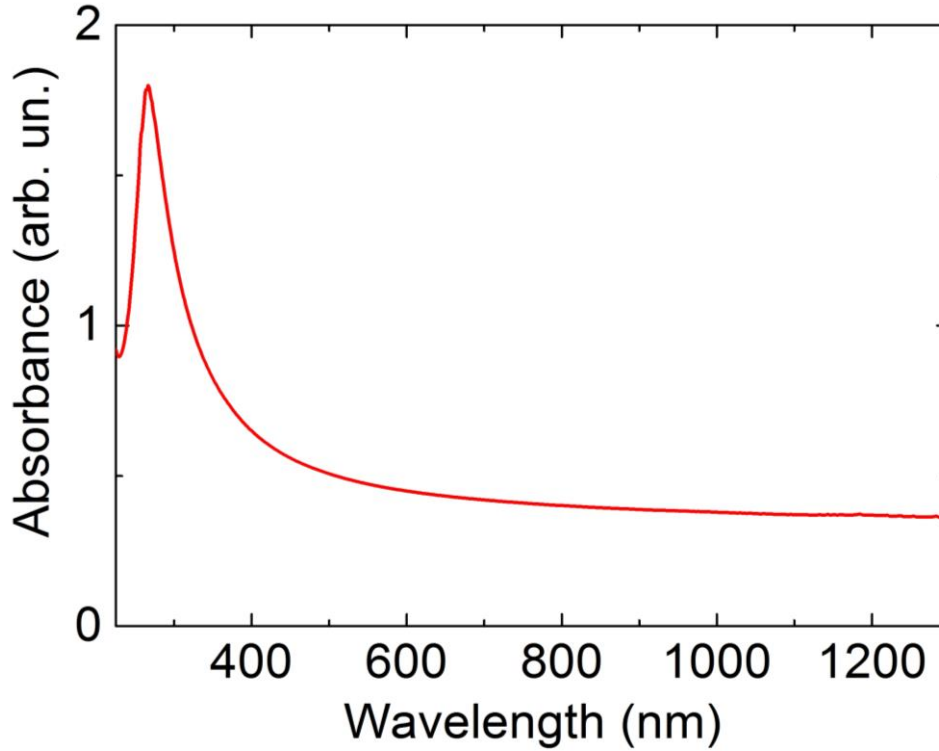


Figure S3: Optical absorption spectrum of graphene dispersion in water with SDC surfactant.

S2.2 Raman Spectroscopy

S2.2.1 Pristine SWNTs

Raman spectroscopy can be used to probe SWNTs within dispersions. In the low frequency region, the Radial Breathing Modes (RBMs) are observed¹⁷. Their position, $\text{Pos}(RBM)$, is inversely related to SWNT diameter, d ^{18,19,20}, as given by

$$\text{Pos}(RBM) = \frac{C_1}{d} + C_2$$

Combining $\text{Pos}(RBM)$, with excitation wavelength and the ‘Kataura plot’^{11,21}, it is, in principle, possible to derive the SWNT chirality^{22,23}.

Matching the diameter with excitation wavelength in the Kataura plot also gives information on the semiconducting or metallic character. A variety of C_1 and C_2 were proposed for this relation^{17,18,19,23,24}. Here we use the $C_1=214.4\text{ cm}^{-1}\text{ nm}$ and $C_2=18.7\text{ cm}^{-1}$, from Ref. 18. These were derived by plotting the resonance energy as a function of inverse RBM frequency without additional assumptions. We also validated our results by using the parameters proposed in Refs. 19, 24, 25.

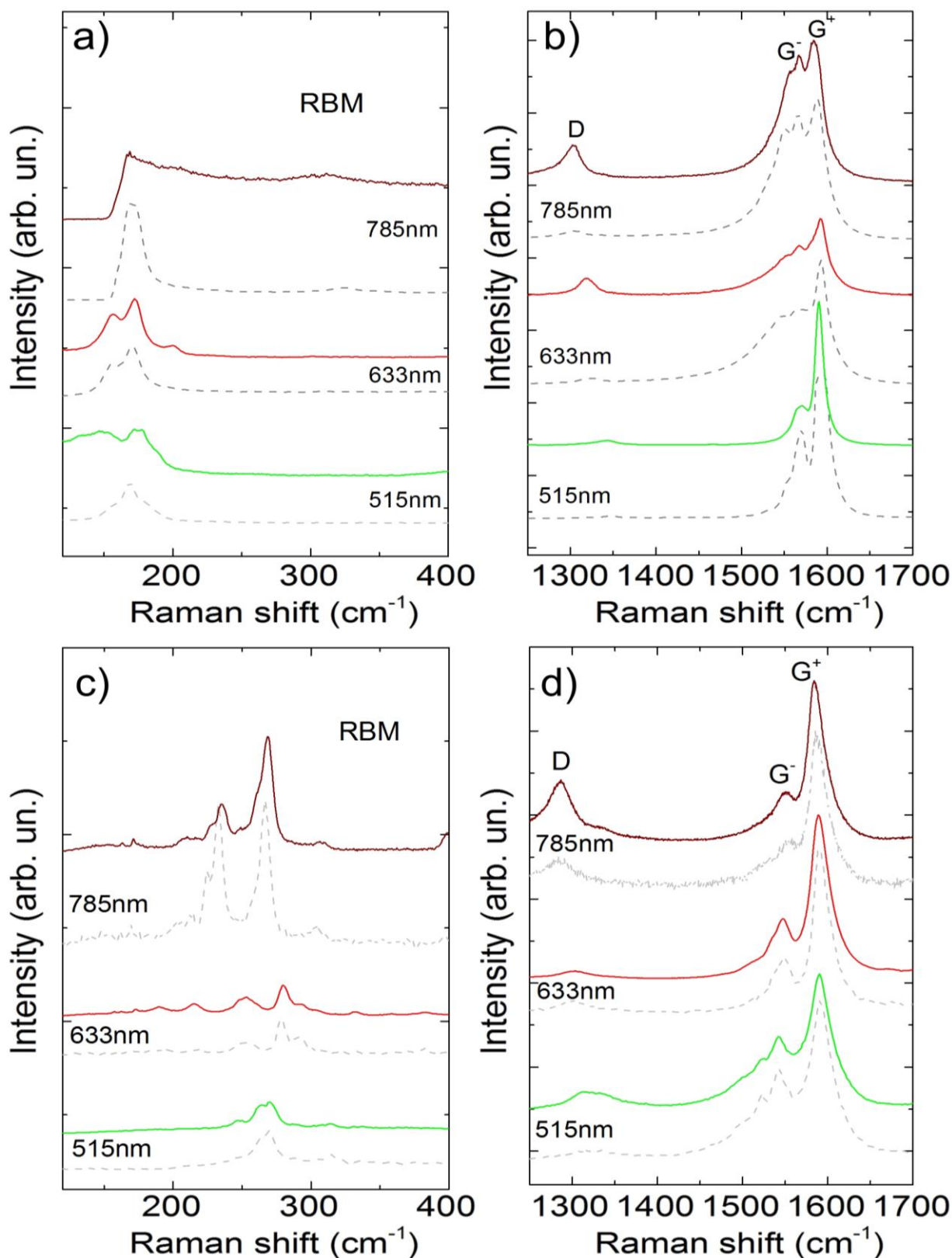


Figure S4: Raman spectra of SWNTs at different excitation wavelengths: 514.5nm (green curve), 633nm (red curve) and 785nm (brown curve) (a) RBM and (b) G region for SWNT-1 and (c) RBM and (d) G region for SWNT-2. The Raman spectra of the starting materials (powders) are reported in light grey dashed lines below each curve for comparison.

Raman spectroscopy also probes possible damage via the D peak²⁶. The D peak is due to the breathing modes of sp^2 rings and requires a defect for its activation by double resonance (DR)^{27,28}. The typical Raman spectrum of SWNTs in the 1500-1600 cm^{-1} region consists of the G^+ and G^- bands. In s-SWNTs, they originate from the longitudinal (LO) and tangential (TO) modes, respectively, derived from the splitting of the E_{2g} phonon of graphene at the Brillouin zone centre^{27,28,29,30,31}. The positions of the G^+ and G^- peaks, $Pos(G^+)$, $Pos(G^-)$, are diameter dependent and their separation increases with decreasing diameter^{32,33}. In m-SWNTs, the assignment of the G^+ and G^- bands is the opposite, and the FWHM of the G^- peak, $FWHM(G^-)$, is larger and $Pos(G^-)$ down-shifted with respect to the semiconducting counterpart^{32,34}. Thus, a wide, low frequency G^- is a fingerprint of m-SWNTs. On the other hand, the absence of such a feature does not necessarily imply that only s-SWNTs are present, but could signify that m-SWNTs are off-resonance.

Doping could also modify positions and FWHMs^{35,36}. In m-SWNTs, a $Pos(G^-)$ blueshift, accompanied by a $FWHM(G^-)$ decrease is observed with electron or hole doping^{37,38}. In s-SWNTs, doping upshifts $Pos(G^+)$, but does not affect $FWHM(G^+)$ ^{35,37}.

Thus, a large number of excitation wavelengths are necessary for a complete characterization of SWNTs^{20,24}. Nevertheless, useful information can be derived even with few excitation wavelengths.

Raman spectra are taken on both the starting materials (powder) and the dispersions, deposited by drop-casting onto an aluminium substrate to avoid any Raman background, with a Renishaw system at 514.5 nm (2.41 eV) 633 nm (1.96 eV) and 785 nm (1.58 eV), using a 100X objective and a less than 1 mW on the sample. The RBM detection is limited by the cut-off of the notch and edge filters. These are at 120, 100 and 110 cm^{-1} for 514, 633 and 785nm, respectively, limiting the detection to diameters up to ~ 1.9 nm.

The RBM spectra of the SWNT-1 in Fig. S4(a) show a distribution, spanning the 175–370 cm^{-1} range both for the starting material and the dispersion, considering the peaks for the three excitation wavelengths. This RBM range corresponds to SWNTs with ~ 0.6 – 1.35 nm diameter. Fig. S4(b) plots the spectra in the G region of SWNT-1. A weak D band is observed [$I(D)/I(G) = 0.13$], indicating small number of defects.^{28,30} These defects could be induced by the ultrasonication process because the $I(D)/I(G) = 0.05$ of the powder is lower with respect to the dispersion.

The RBM spectra of the SWNT-2 in Fig. S4(c) show a similar distribution but peaked at lower wavenumbers with respect to SWNT-1. Indeed, the RBMs span the 150–215 cm^{-1} range both for the starting material and the dispersion, considering the peaks for the three excitation wavelengths. This corresponds to SWNTs with ~ 1.05 – 1.65 nm diameter. Fig. S4(d) plots the spectra in the G region of SWNT-1. A weak D band is also observed [$I(D)/I(G) = 0.18$] for the SWNT-2 sample, indicating small number of defects.^{28,30} As for the SWNT-1, also in the case of the SWNT-2 sample, these defects could be induced by the ultrasonication process because the $I(D)/I(G) = 0.08$ of the powder is lower with respect to the one of the dispersion.

S2.3 Pristine graphene flakes and dispersions

The ultracentrifuged dispersions are drop-cast onto a Si wafer with 300nm thermally grown SiO_2 (LDB Technologies Ltd.). These samples are then used for Raman measurements at 488, 514.5, and 633nm. The G peak dispersion is defined as $Disp(G) = \Delta Pos(G) / \Delta \lambda_L$, where λ_L is the laser excitation wavelength.

Fig. S5a plots a typical Raman spectrum of the flakes prepared on Si/ SiO_2 substrates.

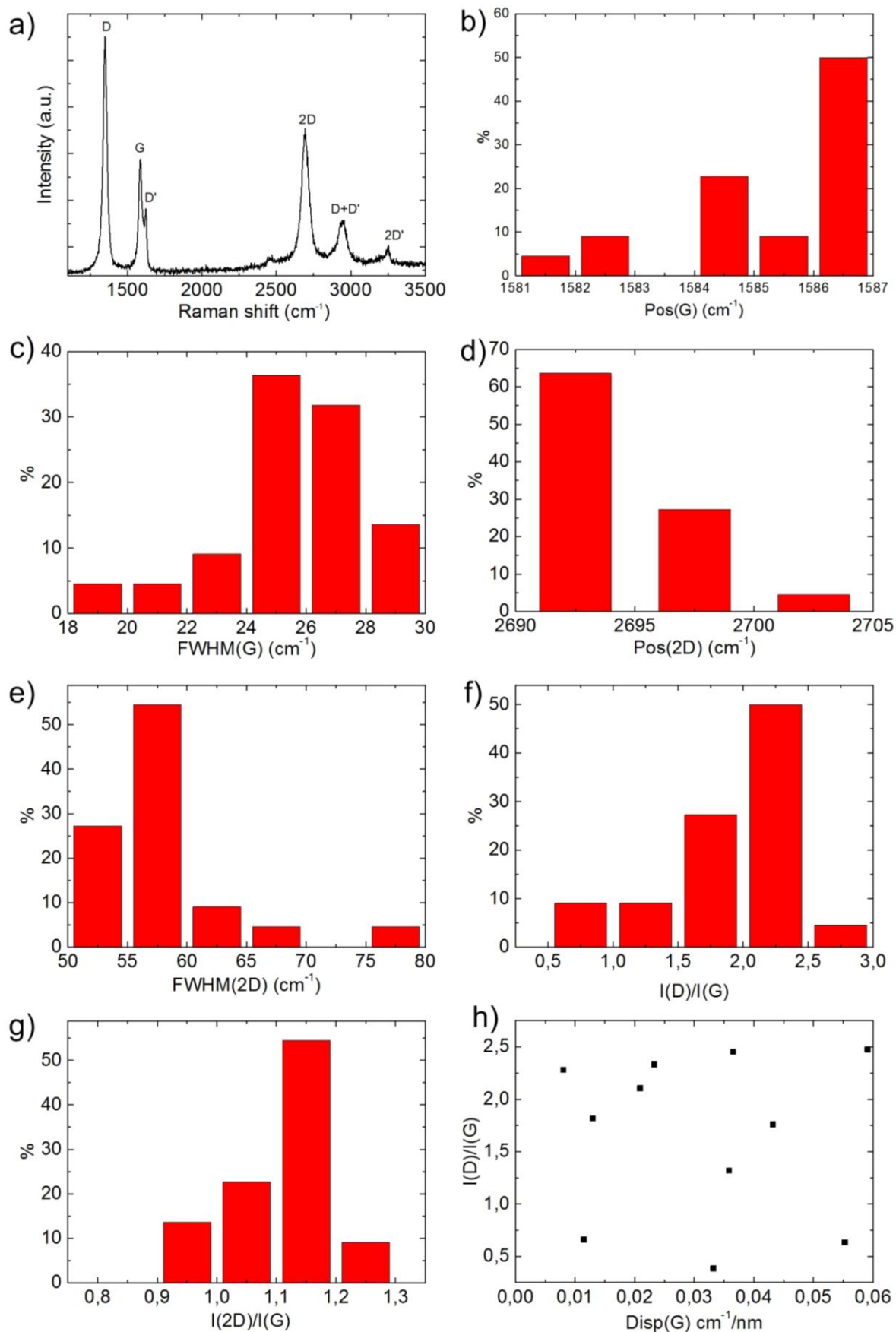


Figure S5: a) Raman spectrum measured at 514.5nm excitation for a representative flake obtained via LPE of graphite. Distribution of b) Pos(2D), c) FWHM(2D), d) Pos(G), e) FWHM(G), f) $I(D)/I(G)$, g) $I(2D)/I(G)$, and h) distribution of $I(D)/I(G)$ as a function of Disp(G).

Besides the G and $2D$ peaks, this spectrum shows significant D and D' intensities and the combination mode $D+D'$. Statistical analysis of the spectra shows that $\text{Pos}(G)$ (Fig. S5b) and $\text{FWHM}(G)$ (Fig. S5c) are ~ 1582 and $\sim 27\text{cm}^{-1}$. $\text{Pos}(2D)$ peaks $\sim 2695\text{cm}^{-1}$ (Fig. S5d), while $\text{FWHM}(2D)$ varies from 50 to 80cm^{-1} (Fig. S5e) with a peak at 57cm^{-1} . This is consistent with the samples being a combination of single- (SLG) and few-layer (FLG) graphene flakes. The Raman spectra show significant D and D' intensities, with the intensity ratio $I(D)/I(G)$ having a maximum at 2.25 (Fig. S5f). This high $I(D)/I(G)$ is attributed to the edges of our sub-micrometer flakes³⁹, rather than to the presence of a large amount of structural defects within the flakes. This observation is supported by the low $\text{Disp}(G) < 0.06\text{ cm}^{-1}/\text{nm}$, much lower than what expected for disordered carbon²⁸. Combining $I(D)/I(G)$ with $\text{Disp}(G)$ allows us to discriminate between disorder localized at the edges and disorder in the bulk. In the latter case, a higher $I(D)/I(G)$ would correspond to higher $\text{Disp}(G)$. Fig. S5h show that $\text{Disp}(G)$ and $I(D)/I(G)$ are not correlated, an indication that the major contribution to the D peak comes from the edges of the sample.

S.3 Nanotensile Tests

Nanotensile tests were performed under controlled laboratory conditions (in the Laboratory of Bio-Inspired and Graphene Nanomechanics of the University of Trento), since any change in temperature and humidity may affect the mechanical characteristics of the silk threads^{2,40,41,42,43}.

We monitored the experimental ambient conditions with a datalogger (EL-USB-2, Lascar Electronics): the air temperature and the relative humidity were recorded to be $22.8 \pm 1.3\text{ }^\circ\text{C}$ and $59.1 \pm 5.0\%$ during tensile tests. We fixed silk fibre ends to $15 \times 10\text{ mm}^2$ “c” shaped cardboard holders, with double adhesive faces. These allowed the fibre to be suspended and mounted on the nanotensile testing machine, while maintaining its original tension without damage (Fig. S6g). The tests were conducted using a nanotensile testing system (T150, Agilent, Santa Clara, USA), equipped with 500 mN maximum cell load. This can generate load-extension data with a load resolution of 50 nN and a 0.1nm displacement resolution. The cardboard holders were placed between the clamps. Once the holders were in place, the clamps were closed and one side of the holders was cut (Fig. S6h), leaving the fibre free between the clamps. We performed a continuous dynamic analysis of the silk by imposing an oscillating dynamic strain up to failure of the thread. We used a dynamic strain oscillation with a 20Hz frequency and a 0.1mN dynamic force amplitude, which enabled mechanical properties to be determined continuously.

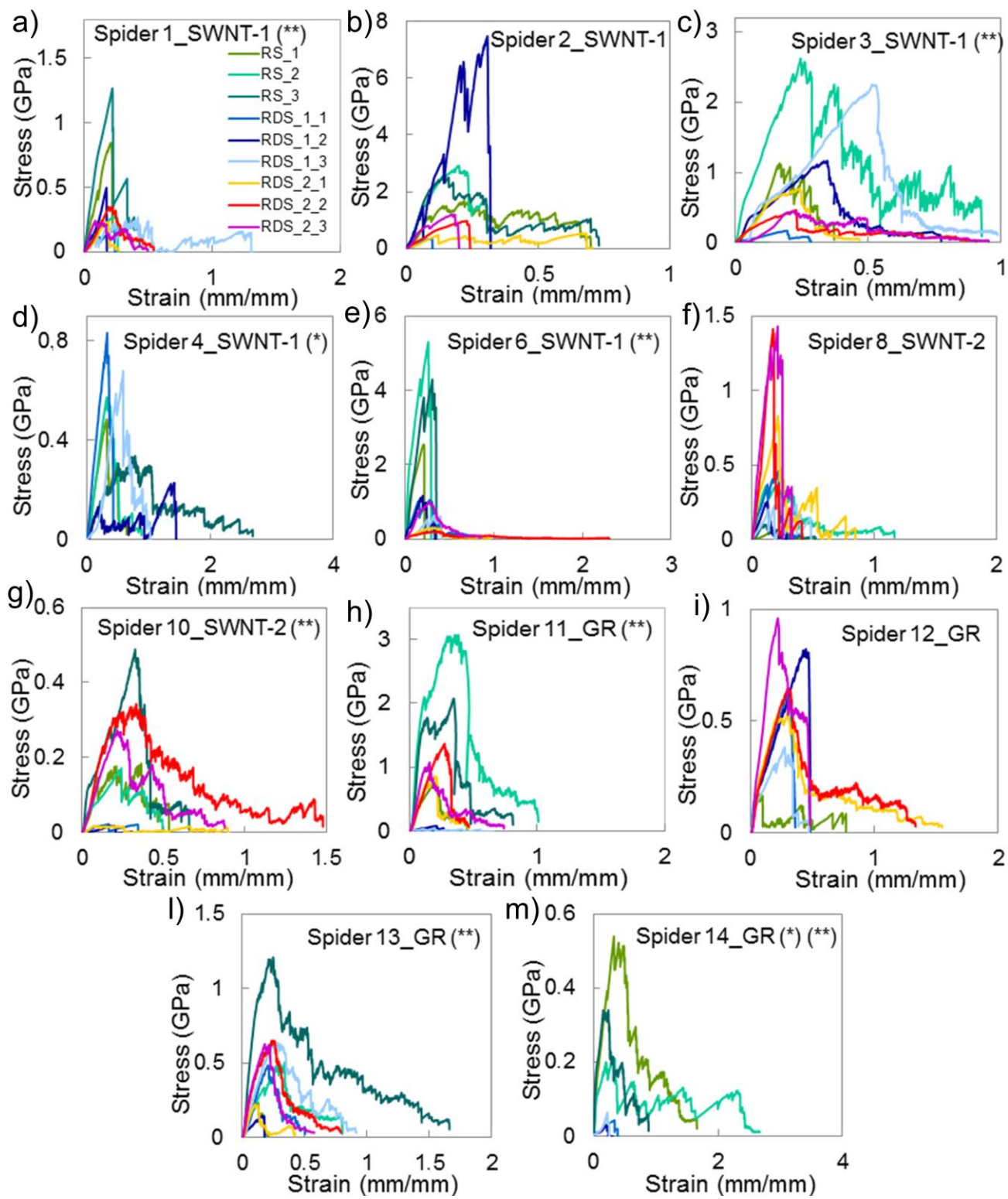


Figure S6: Stress-strain curves. Stress-strain curves for silk produced by spiders after first (RDS₁) or second (RDS₂) ingestion of a-g) SWNT-1, SWNT-2 or h-m) graphene dispersions. The symbol “**” specifies enhanced mechanical properties (fracture strength and Young’s modulus) after first collection. The symbol “*” specifies that spiders died before the second collection. The legend is reported for the Spider1_SWNT-1.

S.4 Atomistic simulations

The three-dimensional structure of the crystalline region of major ampullate spidroin 2 (MASP2) is generated using the (PS)2-v2 program⁴⁴. Simulations are performed using the GROMACS package (version 4.6.3)⁴⁵. The MASP2 protein is simulated using the all-atom AMBER/99 force field.⁴⁶ We generate capped (10,10) nanotubes with a length of 2.1 nm, and squared graphene sheets (with dangling bonds saturated with hydrogen) of size 1.8 x 2.5 nm². Both nanotubes and graphene are simulated using the DREIDING force field⁴⁷ for the bonded interactions, which has been proved to be a good compromise between simplicity and accuracy for carbon allotropes, while Steele parameters are used for the Lennard-Jones carbon interactions as they are more accurate than the original DREIDING ones⁴⁸. The starting configurations are generated by placing 4 nanotubes or 4 graphene sheets around the protein, and pulling them towards MASP2's center of mass. After removing the pulling force, we equilibrated the system for 500 ps, with all the bonds treated as flexible and using a time step of 1 fs as common practice in molecular mechanics simulations of molecules. The resulting configurations are shown in Figs. 6(a,b). We then apply a fixed force F on the two protein terminals and directed along the vector connecting their centers of mass. The computations are run for 500 ps, of which 250 ps are necessary to reach equilibration, and the remaining 250 ps were used to compute average values, such as the end-to-end distance of the MASP2 protein. The force F is varied in the range 50 to 1000 kJ/nm/mol in steps of 50 kJ/nm/mol. The highest value of the force was set in such a way to obtain completely stretched MASP2 configurations.

S.5 Statistical data analysis and numerical HFBM simulations

Analysis of experimental data discussed in the Main Text and in the “Nanotensile Tests” Section indicates that there is a large statistical spread in the measured mechanical properties of RS as well as CNTS and GS. Therefore, to evaluate the effect of SWNT and graphene addition it is necessary to perform a statistical analysis of the experimental data. To do this, we adopt the Weibull distribution, which is widely used in fracture mechanics and particularly suitable to describe dispersion of mechanical properties⁴⁹, and separately fit the data relative to RS, SWNT-1-CNTS, SWNT-2-CNTS and RS. The resulting 2-parameter Weibull distributions are shown in Fig. S7. The parameters for the corresponding Weibull distributions of RS, CNTS and GS are summarized in Table S1. Scale parameters are indicative of average values, whilst shape parameters are correlated to the dispersion of the distributions. The addition of SWNTs leads to an average increase in the stiffness and strength of the silk, and an average reduction in the ultimate strain, whilst the addition of graphene does not improve average stiffness and strength, although it leads to the same decrease in average ultimate strain. In all cases, we get an increase in the dispersion (*i.e.*, decrease in Weibull shape parameters) of the mechanical properties, possibly due to variable reinforcement volume fractions. Numerical simulations of deformation and fracture are performed using a previously developed Hierarchical Fibre Bundle Model (HFBM)⁵⁰, whereby the macroscopic fibres are modelled as networks of microfibres and/or reinforcements arranged in parallel and in series, subjected to uniaxial tension. The microfibers are treated as elastic springs with statistically distributed fracture strengths, according to measured or known input parameters for the constituents (*i.e.* the experimentally-determined Weibull parameters from Table S.1 for the silk, and known mechanical properties from the literature for SWNT and graphene). Simulations are carried out in a multiscale procedure, from single SWNT (diameter ~1.5 nm, length ~250 nm) scale to the macroscopic scale of specimens used in experimental tests (diameter ~ 5 μ m, length ~1 cm). We consider typical values for SWNT and graphene properties, respectively: Young's modulus $E_{\text{CNT}} = E_{\text{G}} = 1 \text{ TPa}^{51,52}$ and strength $\sigma_{\text{CNT}} = 45 \text{ GPa}^{50}$, $\sigma_{\text{G}} = 130 \text{ GPa}^{51}$. The experimentally obtained RS Weibull distributions are used as input properties. Fig. S8 shows typical simulations results for

stress-strain curves with different SWNT volume fractions V_f , assuming a uniform SWNT dispersion at the lowest hierarchical simulation level (i.e. that at which individual SWNTs coincide with springs in the bundle). The figure shows that there is an overall strength and modulus increase with increasing V_f , while there is a corresponding ultimate strain reduction.

Table S1. Mean Young's modulus, strength and ultimate strain of RS, CNTS and GS, and corresponding Weibull parameters.

Young's Modulus	Mean (GPa)	STD (GPa)	Shape parameter	Scale parameter (GPa)
RS	10.73	10.43	1.19	11.06
SWNT-1-CNTS	17.10	15.70	0.99	17.70
SWNT-2-CNTS	17.60	18.89	0.48	14.23
GS	4.44	4.58	0.83	4.32

Strength	Mean (MPa)	STD (MPa)	Shape parameter	Scale parameter (MPa)
RS	1082.94	1082.94	1.27	1126.55
SWNT-1-CNTS	1401.36	1508.48	1.13	1953.83
SWNT-2-CNTS	834.25	2136.60	0.47	1523.46
GS	3299.16	440.94	0.76	486.08

Ultimate Strain	Mean (mm/mm)	STD (mm/mm)	Shape parameter	Scale parameter (mm/mm)
RS	0.70	0.40	2.09	0.79
SWNT-1-CNTS	0.59	0.22	2.16	0.69
SWNT-2-CNTS	0.45	0.17	2.57	0.52
GS	0.40	0.08	4.95	0.43

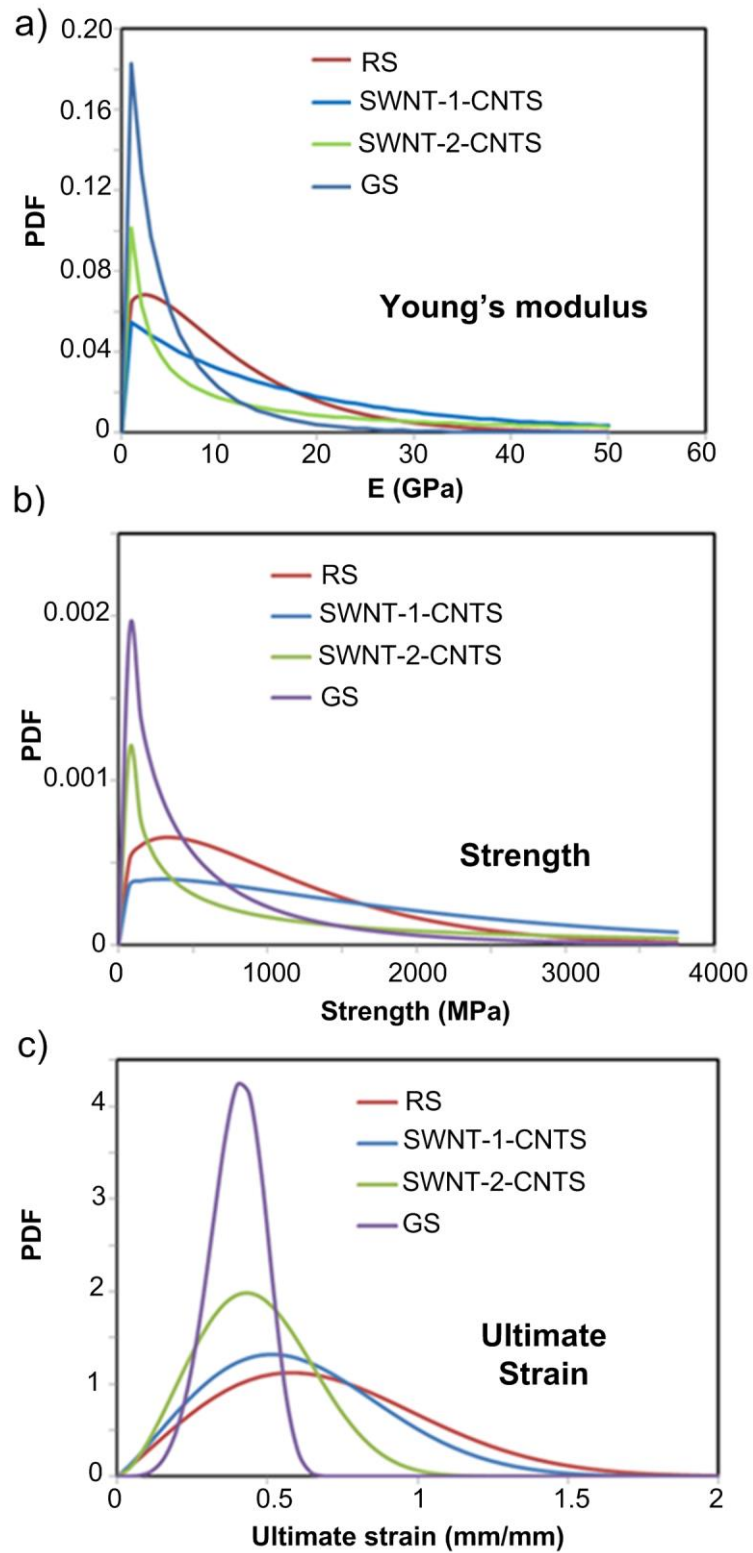


Figure S7: Weibull fits. Weibull fits (Probability Density Functions, PDF) on experimental data for a) Young's modulus, b) strength and c) ultimate strain of RS, CNTS, and GS.

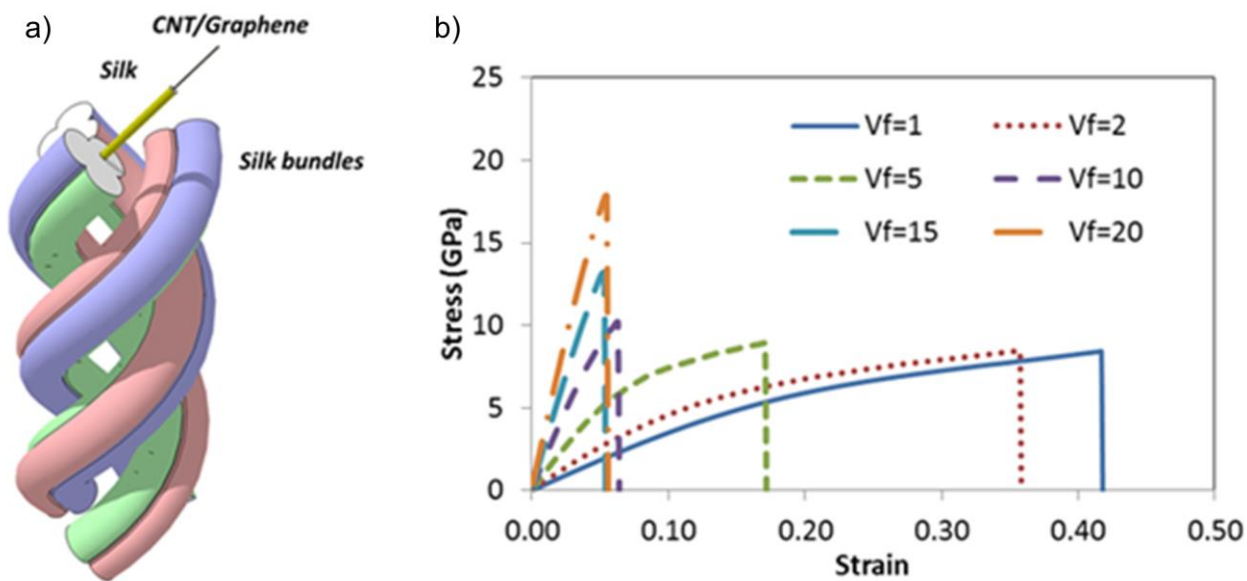


Figure S8: HFBM simulations. a) Schematic of the model and b) examples of stress-strain results for different volume ratios.

References SI

- 1 Guinea, G. V., Elices, M., Perez-Rigueiro, J. & Plaza, G. Self-tightening of spider silk fibers induced by moisture. *Polymer* **44**, 5785–5788 (2003).
- 2 O'Connell, M. *et al.* Band gap fluorescence from individual single-walled carbon nanotubes. *Science* **297**, 593–596 (2002).
- 3 Tan, P. H. *et al.* Photoluminescence spectroscopy of carbon nanotube bundles: Evidence for exciton energy transfer. *Phys. Rev. Lett.* **99**, 137402 (2007).
- 4 Tan, P. H. *et al.* Optical properties of nanotube bundles by photoluminescence excitation and absorption spectroscopy. *Physica E Low Dimens. Syst. Nanostruct.* **40**, 2352–2359 (2008).
- 5 Hagen, A. & Hertel, T. Quantitative analysis of optical spectra from individual single-wall carbon nanotubes. *Nano Letters* **3**, 383–388 (2003).
- 6 Bonaccorso, F. *et al.* Density gradient ultracentrifugation of nanotubes: interplay of bundling and surfactants encapsulation. *J. Phys. Chem. C* **114**, 17267–17285 (2014).
- 7 Krupke, R., Hennrich, F., Hampe, O. & Kappes, M. M. Near-infrared absorbance of single-walled carbon nanotubes dispersed in dimethylformamide. *J. Phys. Chem. B* **107**, 5667–5669 (2003).
- 8 Landi, B. J., Ruf, H. J., Worman, J. J. & Raffaella, R. P. Effects of alkyl amide solvents on the dispersion of single-wall carbon nanotubes. *J. Phys. Chem. B* **108**, 17089–17095 (2004).
- 9 Weisman, R. B. & Bachilo, S. M. Dependence of optical transition energies on structure for single-walled carbon nanotubes in aqueous suspension: An empirical Kataura plot. *Nano Letters* **3**, 1235–1238 (2003).
- 10 Kataura, H. *et al.* Optical properties of single-wall carbon nanotubes. *Synthetic Met.* **103**, 2555–2558 (1999).
- 11 Bachilo, S. *et al.* Structure-assigned optical spectra of single-walled carbon nanotubes. *Science* **298**, 2361–2366 (2002).

-
- 12 Kravets, V. G. *et al.* Spectroscopic ellipsometry of graphene and an exciton-shifted van Hove peak in absorption. *Phys. Rev. B* **81**, 155413 (2010).
- 13 Hasan, T. *et al.* Solution-phase exfoliation of graphite for ultrafast photonics. *Phys. Status Solidi B* **247**, 2953–2957 (2010).
- 14 Torrisi, F. *et al.* Inkjet-printed graphene electronics. *ACS Nano* **6**, 2992 (2012).
- 15 Hernandez, Y. *et al.* High-yield production of graphene by liquid-phase exfoliation of graphite. *Nat. Nanotech.* **3**, 563–568 (2008).
- 16 Rao, A. M. *et al.* Diameter-selective Raman scattering from vibrational modes in carbon nanotubes. *Science* **275**, 187–191 (1997).
- 17 Telg, H., Maultzsch, J., Reich, S., Hennrich, F. & Thomsen, C. Chirality distribution and transition energies of carbon nanotubes. *Phys. Rev. Lett.* **93**, 177401 (2004).
- 18 Meyer, J. C. *et al.* Raman modes of index-identified freestanding single-walled carbon nanotubes. *Phys. Rev. Lett.* **95**, 075401 (2005).
- 19 Fantini, C. *et al.* Optical transition energies for carbon nanotubes from resonant Raman spectroscopy: Environment and temperature effects. *Phys. Rev. Lett.* **93**, 147406 (2004).
- 20 Weisman, R. B. & Bachilo, S. M. Dependence of optical transition energies on structure for single-walled carbon nanotubes in aqueous suspension: An empirical Kataura plot. *Nano Letters* **3**, 1235–1238 (2003).
- 21 Paillet, M. *et al.* Raman active phonons of identified semiconducting single-walled carbon nanotubes. *Phys. Rev. Lett.* **96**, 257401 (2006).
- 22 Jorio, A. *et al.* Structural (n, m) determination of isolated single-wall carbon nanotubes by resonant Raman scattering. *Phys. Rev. Lett.* **86**, 1118–1121 (2001).
- 23 Araujo, P. T. *et al.* Third and fourth optical transitions in semiconducting carbon nanotubes. *Phys. Rev. Lett.* **98** (2007).
- 24 Araujo, P. T., Jorio, A., Dresselhaus, M. S., Sato, K. & Saito, R. Diameter dependence of the dielectric constant for the excitonic transition energy of single-wall carbon nanotubes. *Phys. Rev. Lett.* **103** (2009).
- 25 Ferrari, A. C. Raman spectroscopy of graphene and graphite: Disorder, electron-phonon coupling, doping and nonadiabatic effects. *Solid State Commun.* **143**, 47–57 (2007).
- 26 Ferrari, A. C. *et al.* Raman Spectrum of Graphene and Graphene Layers. *Phys. Rev. Lett.* **97**, 187401 (2006).
- 27 Ferrari, A. C. & Robertson, J. Interpretation of Raman spectra of disordered and amorphous carbon. *Phys. Rev. B* **61**, 14095–14107 (2000).
- 28 Tuinstra, F. & Koenig, J. L. Raman spectrum of graphite. *J. Chem. Phys.* **53**, 1126 (1970).
- 29 Ferrari, A. C. & Basko, D. Raman spectroscopy as a versatile tool for studying the properties of graphene. *Nat. Nanotech.* **8**, 235–246 (2013).
- 30 Mohiuddin, T. M. G. *et al.* Uniaxial strain in graphene by Raman spectroscopy: G peak splitting, Gruneisen parameters, and sample orientation. *Phys. Rev. B* **79**, 205433 (2009).
- 31 Piscanec, S., Lazzeri, M., Robertson, J., Ferrari, A. C. & Mauri, F. Optical phonons in carbon nanotubes: Kohn anomalies, Peierls distortions, and dynamic effects. *Phys. Rev. B* **75**, 035427 (2007).
- 32 Jorio, A. *et al.* G-band resonant Raman study of 62 isolated single-wall carbon nanotubes. *Phys. Rev. B* **65**, 155412 (2002).
- 33 Lazzeri, M., Piscanec, S., Mauri, F., Ferrari, A. C. & Robertson, J. Phonon linewidths and electron-phonon coupling in graphite and nanotubes. *Phys. Rev. B* **73**, 155426 (2006).
- 34 Tsang, J.C., Freitag, M., Perebeinos, V., Liu, J. & Avouris, P. Doping and phonon renormalization in carbon nanotubes. *Nat. Nanotechnol.* **2**, 725–730 (2007).
- 35 Das, A. *et al.* Monitoring dopants by Raman scattering in an electrochemically top-gated graphene transistor. *Nat. Nanotechnol.* **3**, 210–215 (2008).

-
- 36 Das, A. *et al.* Doping in carbon nanotubes probed by Raman and transport measurements. *Phys. Rev. Lett.* **99**, 136803 (2007).
- 37 Shiozawa, H. *et al.* Screening the missing electron: nanochemistry in action. *Phys. Rev. Lett.* **102**, 046804 (2009).
- 38 Casiraghi, C. *et al.* Rayleigh imaging of graphene and graphene layers. *Nano Lett.* **7**, 2711–2717 (2007).
- 39 Brown, C. P. *et al.* The critical role of water in spider silk and its consequence for protein mechanics. *Nanoscale* **3**, 3805–3811 (2011).
- 40 Agnarsson, I., Dhinojwala, A., Sahni, V. & Blackledge, T. A. Spider silk as a novel high performance biomimetic muscle driven by humidity. *J. Exp. Biol.* **212**, 1990–1994 (2009).
- 41 Vollrath, F., Madsen, B. & Shao, Z., The effect of spinning conditions on the mechanics of a spider's dragline silk. *Proc. R. Soc. Lond. B* **268**, 2339–2346 (2001).
- 42 Liu, Y., Shao, Z. & Vollrath, F., Relationships between supercontraction and mechanical properties of spider silk. *Nat. mater.* **4**, 901–905 (2005).
- 43 Chen, C.-C., Hwang, J.-K. & Yang, J.-M. (PS)2-v2: template-based protein structure prediction server. *BMC Bioinformatics* **10**, 366 (2009).
- 44 Hess, B., Kutzner, C., Van der Spoel, D. & Lind, E. GROMACS 4: algorithms for highly efficient, load-balanced, and scalable molecular simulation. *J. Chem. Theory Comput.* **4**, 435–447 (2008).
- 45 Lindorff-Larsen, K. *et al.* Improved side-chain torsion potentials for the Amber ff99SB protein force field. *Proteins* **78**, 1950–1958 (2010).
- 46 Mayo, S. L., Olafson, B. D. & Goddard, W. A. DREIDING: a generic force field for molecular simulations. *J. Phys. Chem.* **94**, 8897–8909 (1990).
- 47 Steele W. A. The interaction of rare gas atoms with graphitized carbon black. *J. Phys. Chem.* **82**, 817–821 (1978).
- 48 Weibull, W. A statistical distribution function of wide applicability. *J. Appl. Mech.* **18**, 293–297 (1951).
- 49 Pugno, N. M., Bosia, F. & Carpinteri A. Multiscale stochastic simulations for tensile testing of nanotube-based macroscopic cables. *Small* **4**, 1044–1052 (2008).
- 50 Ruoff, R. S., Qian, D. & Liu, W. K., Mechanical properties of carbon nanotubes: theoretical predictions and experimental measurements. *C. R. Physique* **4**, 993–1008 (2003).
- 51 Lee, C., Wei, X., Kysar, J. W. & Hone, J. Measurement of the elastic properties and intrinsic strength of monolayer graphene. *Science* **321**, 385–388 (2008).